Luminescent Properties of Anthracene-based Metal-Organic Frameworks

Jennifer Maria Rowe

Thesis submitted to the faculty of the Virginia Polytechnic Institute and State University in partial fulfillment of the requirements for the degree of

Master of Science

In

Chemistry

Amanda J. Morris, Chair

Brian M. Tissue

John Morris

May 6, 2016

Blacksburg, VA

Key words: Metal-Organic Frameworks, luminescence, photophysics, anthracene

Luminescent Properties of Anthracene-based Metal-Organic Frameworks

Jennifer Maria Rowe

Abstract: Metal-organic frameworks (MOFs) are crystalline materials composed of metal clusters and organic ligands. MOFs that exhibit photoluminescence are promising materials for a broad range of applications. Due to their structural tunability and crystalline nature, luminescent MOFs also provide an excellent platform for studying structure–property relationships of materials.

The photophysical properties of three anthracene-dicarboxylic acids – 1,4-anthracene dicarboxylic acid (1,4-ADCA), 2,6-anthracene dicarboxylic acid (2,6-ADCA) and 9,10-anthracene dicarboxylic acid (9,10-ADCA) – were studied in a series of polar aprotic solvents using steady-state absorption, steady-state emission spectroscopy and time-correlated single photon counting (TCSPC) emission lifetime spectroscopy. The addition of carboxylic acid functional groups on the anthracene ring alters photophysical properties to varying degrees depending on the location and protonation state. Density functional theory (DFT) calculations reveal that the lowest-energy ground-state structures of both 2,6-ADCA and 1,4-ADCA have dihedral angles between the carboxylic acids and aromatic planes of $\theta = 0°$, while the same dihedral angle increases to $\theta = 56.6°$ for 9,10-ADCA. Time-dependent DFT calculations suggest that the carboxyl groups of 1,4-ADCA and 2,6-ADCA remain coplanar with the anthracene ring system in the excited state. In contrast, the calculations reveal significant changes between the ground and excited geometries for 9,10-ADCA and puckering of the anthracene moiety of is observed.

The three anthracene dicarboxylic acids were then incorporated into zirconium-based MOFs. The MOF structures were characterized using powder X-ray diffraction (PXRD) and scanning electron microscopy (SEM). The steady-state absorption and emission spectra as well as the fluorescence lifetimes of the MOFs were compared to that of the corresponding ligand in solution. The MOFs comprising 9,10-ADCA and 2,6-ADCA formed highly crystalline octahedral shaped crystals and were found to be isostructural with the well-known UiO-66 and UiO-67 frameworks. However, incorporation of the 1,4-ADCA ligand resulted in large rod-shaped crystals. The absorption spectra of the MOFs are broadened and redshifted compared with that of the corresponding free ligands. The emission spectra of the MOFs constructed from 9,10-ADCA and 1,4-ADCA display emission bands that resemble that of the free ligand in acidic solutions, but are slightly broadened and redshifted in the MOF. Little difference is observed between that of 2,6-ADCA within the MOF and in acidic solution. The broadening and redshift observed in the absorption and emission is indicative of intermolecular interactions between anthracene units and/or with the Zr^{4+} clusters. The fluorescence lifetimes measured for the anthracene-based MOFs show a long component, comparable to the lifetime of the free ligand, along with shorter component. This may also suggest intermolecular interactions between chromophores in the MOFs.

Altogether, derivatization of anthracene was shown to have specific effects on the photophysical properties of the parent anthracene molecule. These properties are further altered when the ligand is incorporated into a metal organic framework. Such systematic studies can provide a guide in designing luminescent MOFs with the excited-state properties desired for a given application.

Acknowledgements

First, I would like to thank my advisor, Dr. Amanda Morris. Thank you for not only pushing me to work hard and to do my best, but providing guidance and encouragement along the way. Thank you for believing in me and taking me in as a third-year graduate student. I am very appreciative of all that you have taught me. I also want to thank Dr. Brian Tissue, who co-advised me along with Dr. Karen Brewer during my first years of graduate school. Thank you for your guidance and your patience with me as a new graduate student as well as your continued support for me. I would like to express my gratitude to Dr. John Morris. I appreciate your feedback and the helpful discussions you have provided as my committee member. I also want to thank Dr. David Kingston. I am very grateful for your input as a member of my committee in my first three years as well as the spiritual guidance and encouragement you have offered.

I owe a tremendous amount of gratitude to Dr. William Maza. Thank you for your guidance, your willingness to help and all that you taught me when I was starting out in the Morris group. Thank you as well for your contributions to this project. Also to Jennifer Hay, thank you so much for your help with the organic synthesis as well as your feedback and contributions to the project. I am so grateful for your encouragement and our friendship. I also wish to extend my gratitude to the members of the Morris group and previous Brewer group members; I have gained so much from your helpful discussion, feedback, and support over these past years. To Dr. Elise Naughton, I am extremely thankful for your friendship and support and for always helping me to laugh through some of the tough times in graduate school. To Nathan Carter, I owe an enormous amount of gratitude to you for your constant love and support you have given me over the past few years.

Finally, I wish to express my immense gratitude to my parents, Ronald and Jannell Rowe. I am tremendously grateful for the support and encouragement you've provided me during graduate school. I would not have accomplished so much if not for the constant love and guidance you have provided me throughout my life.

In memory of Dr. Karen Brewer

Table of Contents

Attributions

Chapter 1 of this thesis was adapted from a manuscript recently submitted to *The Journal of Photochemistry C.* Jennifer Hay, a former M.S. student of Dr. Amanda Morris, synthesized the anthracene-based ligands and performed many initial spectroscopic measurements of the compounds. She, along with Dr. William Maza, a previous post-doctoral researcher in the Morris group, contributed to the experimental design, analysis of data and manuscript writing.

Dr. Diego Troya performed the excited state TDDFT calculations of the anthracene derivatives and contributed to writing this section of the manuscript. His graduate student, Robert Chapleski performed ground state DFT calculations of the molecules.

1. Introduction

1.1. Anthracene Photophysics

1.1.1. Photophysical Processes

Anthracene is a polycyclic aromatic hydrocarbon and well-known organic fluorophore composed of three linearly fused benzene rings. Due to its synthetic accessibility and unique photophysical properties, anthracene and its derivatives have been extensively studied since its discovery in 1832.[1] The excited-state properties of anthracene can be fine-tuned through synthetic modification, lending it to a wide range of applications. The photophysical and charge-transport properties of anthracene derivatives have led to its widespread applications in the development of optoelectronics devices such as organic light-emitting diodes (OLEDs), and organic field-effect transistors (OFETs) as well as in photocatalysts and fluorescence sensors.[2]

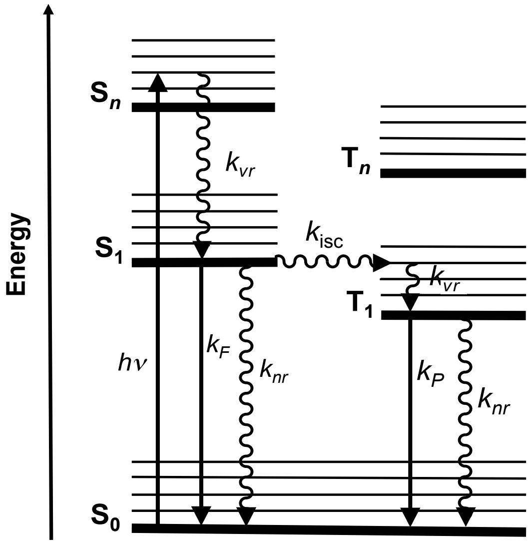

Figure 1.1.1. Jablonski diagram illustrating the excited states transitions upon absorption of a photon of light (hn) where S_0 represents the ground state, S_1 and S_2 represent the singlet excited states, T_1 and T_2 the triplet excited states, k_r = non-radiative decay rate constant, k_{vr} = vibrational relaxation rate constant, k_f = fluorescence, k_{isc} = intersystem crossing rate constant, k_p = phosphorescence rate constant and k_r = the reaction rate constant.

Upon absorption of a photon of the appropriate energy, a molecule is promoted from its singlet ground state, to a singlet excited state. The excited state of the molecule is metastable and can undergo deactivation through several different mechanisms (Figure 1.1.1). This occurs most frequently through intramolecular radiative and non-radiative deactivations and can also occur through intermolecular chemical reactions. The three competing processes of intramolecular excited-state deactivation are non-radiative decay to the ground state (internal conversion, IC); radiative decay to the ground state (fluorescence); and intersystem crossing (ISC) to the triplet state, which involves a change in spin multiplicity. After ISC, T_1 can be deactivated through non-radiative (internal conversion) or radiative (phosphorescence) decay to the ground state.[3]

The probability of an electronic transition is expressed by the magnitude of the oscillator strength of the transition (*f*), which is proportional to the integral of the transition dipole moment. given by equation 1.1, where μ is the transition moment dipole operator and Ψ^{GS} and Ψ^{ES} are the wavefunctions of the ground state and excited state, respectively.

$$\int \Psi^{\mathrm{GS}} \mu \Psi^{\mathrm{ES}} \, \mathrm{d}\upsilon \tag{1.1}$$

Electronic transitions are governed by the spin and the symmetry selection rules. The spin selection rule states that electron spin multiplicity is maintained during a transition. Thus, S → T transitions are formally forbidden, however, they can become partially allowed due to spin-orbit coupling. The symmetry selection rule dictates that the integral of the transition moment must be non-zero and must contain the totally symmetric representation of the group, i.e. a change in dipole must occur. However, such transitions are observed due to vibrations, which distort the molecular symmetry, allowing the wavefunctions to mix. Transitions that are both symmetry and spin allowed will give rise to intense bands in the absorption spectrum with high molar absorptivities while transitions that are only partially allowed will appear as bands with much lower molar absorptivities.[4]

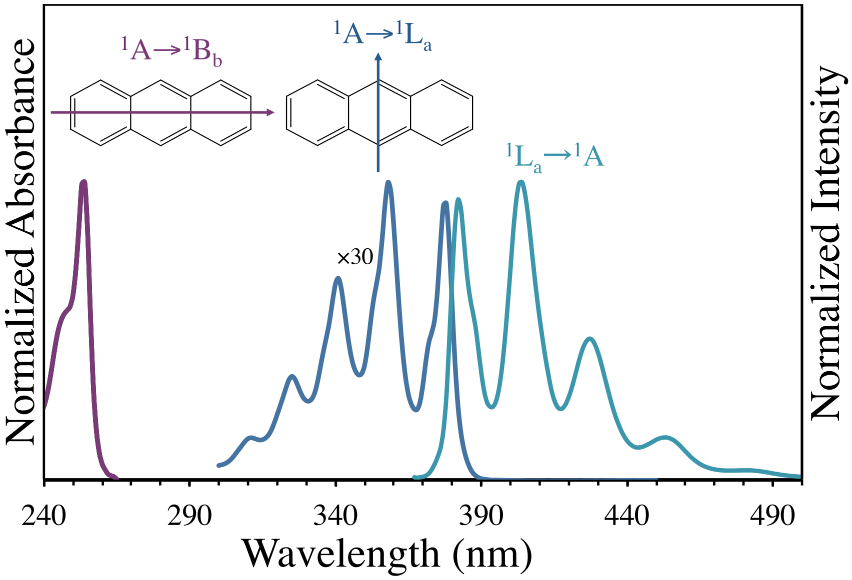

Figure 1.1.2. Absorbance spectrum of anthracene in THF showing the π→π* transitions with dipole moments oriented along the long axis ($^1A \rightarrow ^1B_b$, purple) and across the short axis ($^1A \rightarrow ^1L_a$, dark blue) of anthracene and emission spectrum arising from the $^1L_a \rightarrow ^1A$ transition (light blue).

The absorption spectrum of anthracene (Figure 1.1.2) is characterized by two sets of bands in the 220 – 280 nm and 290 – 400 nm ranges, corresponding to three different π→π* transitions. The absorption observed in each region displays vibronic structure and correspond to one of two transition moments oriented along the molecular axes. The transition dipole of the low-energy transition centered around 256 nm, corresponding to a $^1A \rightarrow ^1B_b$ transition (Platt notation),[5] is polarized along the long axis. The low-energy transition centered around 386 nm, corresponding to a $^1A \rightarrow ^1L_a$ transition, is polarized along the short axis, as illustrated in Figure 1.1.2.[6,7,8] Another longitudinally polarized transition of $^1A \rightarrow ^1L_b$ character is also present, however, the oscillator strength of this transition is weak and is obscured by the much more intense $^1A \rightarrow ^1L_a$ transition band. The mirror image relationship observed between the $^1A \rightarrow ^1L_a$ absorption bands and the $^1L_a \rightarrow ^1A$ emission band is indicative of a negligible change in the nuclear coordinates between the

^1A ground state and ^1L_a excited state from which the emission originates.[9] Thus, according to the Frank-Condon Principle, the geometry of the excited state of anthracene is similar to that of the ground state.[3] When the overlap integral between vibrational levels is large, the molecule can quickly relax through IC, however, the rate of fluorescence can compete with IC when the overlap integral is large. Kasha's rule states that photon emission occurs only from the lowest excited state therefore; emission wavelength is independent of excitation wavelength in most cases. The positions of both the steady-state absorption and emission bands of anthracene are independent of solvent at room temperature.[10] Non-radiative energy losses give rise to a Stokes shift, which is describes the energy gap between the lowest energy maximum of the absorption spectrum and the highest energy maximum of the emission spectrum. Anthracene displays a Stokes shift of 0.0248 eV in cyclohexane at room temperature.[11] Light activated processes are described in terms of quantum yields (equation 1.1) and excited state lifetimes (equation 1.2) The quantum yield (Φ) is a measure of the efficiency of a process and for emission it is the number of photons emitted over the number of photons absorbed. The excited state lifetime (τ) is the amount of time a molecule is in the excited state and is given by the inverse of the rate constants of all pathways of deactivation.[12]

$$\Phi = \frac{k_r}{k_r + k_{nr} + k_{rxn}} \tag{1.2}$$

$$\tau = \frac{1}{k_r + k_{nr} + k_{rxn}} \tag{1.3}$$

The fluorescence quantum yield (Φ_{fl}) and fluorescence lifetime (τ_{fl}) of anthracene are largely insensitive to changes in solvation environment at room temperature.[4, 13] For example, the fluorescence lifetimes measured in benzene, cyclohexane and ethanol are 4.29 ns, 5.24 ns, and 5.1

ns, respectively and the quantum yield of fluorescence is between 0.27 and 0.36 in the same solvents 4.29.[14] The fluorescence and phosphorescence quantum yields of anthracene were studied in polymethylmethacrylate at temperatures ranging from 77 K to 298 K. A decrease in the fluorescence quantum yields was observed as temperature decreased, which was attributed to an increase in the rate of the competing process of intersystem crossing, k_{ISC}, as the rate of fluorescence, k_f, showed only negligible temperature dependence.[15]

The singlet excited state of anthracene undergoes ISC to the triplet excited state with a quantum efficiency of ~ 0.7 and a rate of $\sim 6 \times 10^7$ s^{-1}. The quantum yield of fluorescence is ~ 0.3 and the rate of fluorescence decay is $\sim 1 \times 10^8$ s^{-1}.[16] Thus, the amount of energy lost through internal conversion ($k_{ic} \sim 1 \times 10^6$ s^{-1}) in the singlet excited state is negligible. The rate of radiative decay from the triplet state is much slower ($k_{r,p} = 1.46 \times 10^8$ s^{-1}) than that of internal conversion ($k_{ic} = 1.2 \times 10^6$ s^{-1}).[16-17] Thus, non-radiative decay processes, such as intramolecular vibrations and solvent collisions outcompete radiative emission from the triplet excited state and phosphorescence is not observed in room temperature solutions. Phosphorescence from organic fluorophores is usually measured at cryogenic temperatures to reduce non-radiative decay rates. Recently, a method of measuring the room-temperature phosphorescence from anthracene was reported. The chromophore was embedded in a solid matrix of poly(4-bromostyrene), allowing for control of the modes of ISC, and the triplet excited-state lifetime was found to be 8 ms.[18]

1.1.2. Singlet Fission

Anthracene can be promoted directly into the triplet state through singlet fission (SF). SF is a process in which a chromophore in the singlet excited state energetically couples with a nearby chromophore in the ground state and produces two triplet excited states. Although first reported by Schnider *et al* in 1965, this process has captured the interest of researchers in recent years as a means to overcome the Shockley-Quisser limit of single junction solar cell from, of ~ 31% to 44.2%.[19,20] Because multiple excitons are generated from the absorption of one photon, SF systems with quantum yield greater than 100% have been reported.[21] Additionally, direct promotion to the triplet state avoids the energy losses that result from relaxation of the singlet excited state. Singlet fission between two anthracene molecules is believed to occur via an electron exchange mechanism between an anthracene molecule in its singlet excited state and a neighboring anthracene in the ground state, resulting in two triplet excited state molecules, as illustrated in Figure 1.1.3. Specific conditions must be met in order for the appropriate interchromophore interaction leading to singlet-fission to occur. Although some aspects of the SF mechanism have yet to be elucidated, several of the energetic requirements have been identified. First, the process of SF must outcompete other S_1 deactivation pathways, including IC, ISC, fluorescence or other intermolecular interactions. Additionally, the $S_1 - S_0$ energy must be at least two times that of the $S_0 - T_1$ transition (for anthracene $1E(S_1) = 3.13$ eV and $2E(T_1) = 3.66$ eV).[22] An appropriate strength of coupling is also important, and more efficient SF has been observed in crystals compared with covalently linked chromophores.[23] Furthermore, crystal packing plays an essential role in SF and topology has a significant impact on the SF rate. Recent studies of SF in polyacenene thin films have shown that defect sites in more amorphous films led to increased rates of SF relative to the crystalline films.[24] Currently, research efforts involving SF in polyacenes systems are focused on understanding the differences between the SF mechanisms in molecular crystals and single molecules, optimization of morphology and achieving appropriate chromophore coupling for sufficient charge separation.[22]

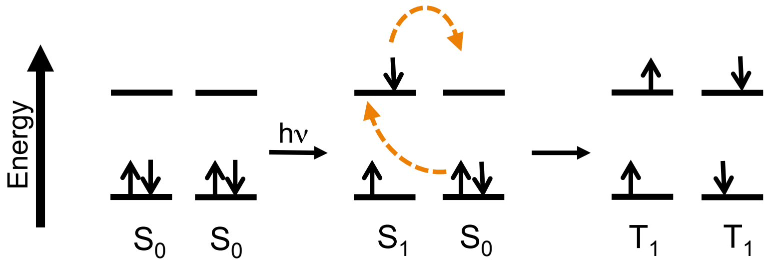

Figure 1.1.3. General mechanism of singlet fission in anthracene

1.1.3. Triplet-Triplet Annihilation (TTA)

The inverse process of SF, triplet-triplet annihilation (TTA), has also been observed in anthracene and several of its derivatives.[25] TTA occurs when two neighboring chromophores in their triplet excited states, interacts to produce one singlet excited state. TTA can be sensitized using a donor molecule that undergoes triplet-triplet energy transfer (TTET) to the triplet excited state of an acceptor molecule. These processes are summarized in a Jablonski diagram in Figure 1.1.4. This phenomenon was first observed by Parker and Hatchard in 1962 in a solution of phenanthrene and anthracene. Efficient TTA-based photon upconversion requires a sensitizer molecule that absorbs visible to near IR light and has a relatively long-lived triplet excited state. Metal-to-ligand charge transfer (MLCT) complexes or metallated porphyrins with strong spin-orbit coupling are ideal candidates due to their efficient intersystem crossing and high triplet quantum yields. Additionally, the acceptor molecules should have a high Φ_F and a triplet state lower in energy than that of the sensitizer, while the energy of the singlet state should be higher that of the sensitizer.[26] Fluorescence upconversion has applications in photovoltaics as well as photocatalysis, lasers, optoelectronics, photodynamic therapy and bioimaging.[27] Castellano *et al* first reported bimolecular TTA-based upconversion in solutions of $[Ru(dmb)_2(bpy\text{-}An)]^{2+}$ (dmb = 4,4′-dimethyl-2,2′-bipyridine, bpy-An = 4-methyl-4′-(9-anthrylethyl)-2,2′-bipyridine).[28] In this complex, the triplet MLCT excited state is higher in energy than the triplet excited state of anthracene and can undergo TTET to anthracene. In this system, intramolecular quenching of the anthracene singlet excited state by the MLCT ground state was observed. Higher upconversion efficiency was observed in solutions of $[Ru(dmb)_3]^{2+}$ and anthracene, in which the donor and acceptor were non-covalently linked. When anthracene was replaced with the derivative, 9,10-diphenyl anthracene (9,10-DPA) further improvement of upconversion efficiency was observed. This was attributed to the higher fluorescence quantum yield of 9,10-DPA (0.95) relative to anthracene (0.27).

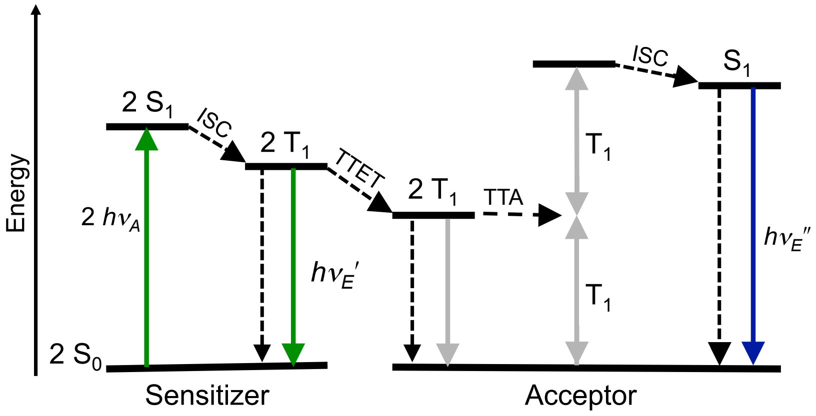

Figure 1.1.4. General energy diagram of fluorescence upconversion via triplet-triplet annihilation (TTA). (TTA). S_0 is the ground state, S_1 and T_1 are the lowest energy, singlet and triplet excited states, respectively, hvA is absorption, hvE′ is phosphorescence from the sensitizer, hv″ is fluorescence from the acceptor, ISC is intersystem crossing, TTET is triplet-triplet energy transfer, TTA is triplet-triplet annihilation.

In fairly concentrated solutions (~ 0.01 M), anthracene is known to photodimerize upon irradiation with UV light (Figure 1.1.5).[29] The [4+4] dimer forms clear crystals that thermally revert back to anthracene at room temperature or when exposed to > 300 nm light.[29] The process of photodimerization occurs through the singlet excited state. This is illustrated by the quenching of photodimerization of anthracene in heavy atom solvents, where ISC to T_1 is enhanced. Since dimerization decreases as T_1 increases it must not be a triplet process. Earlier studies showed that anthracene photodimerization proceeds via TTA.[30] Later, Castellano *et al* demonstrated anthracene photodimerization through TTA upconversion with 514.5 nm irradiation of solutions ~1.4x10-2

M anthracene and 5.25x10-5 M $[Ru(dmb)_3]^{2+}$ in acetonitrile.[31] The reversible bonding properties of anthracene and the high reactivity of the 9 and 10 positions are the basis for many anthracene derivatives. Anthracene oxidation readily yields 9,10-anthraquinone and electrophilic substitution occurs at the 9 and 10 positions. Hence, mono- and di-substitutions in the 9 and 10 positions of anthracene are most common.

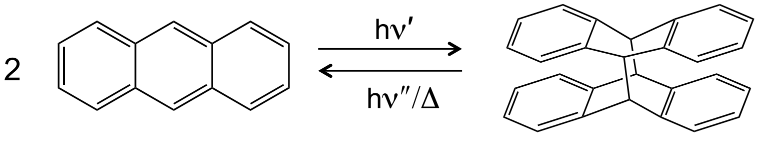

Figure 1.1.5. Photoinduced dimerization of anthracene

The [4+4] dimer is characterized by an absorption spectrum different from that of monomeric anthracene. Anthracene may also form an unstable, excited-state dimer, or excimer. In this case, the absorption spectrum of anthracene does not change, while the emission spectrum appears as a broad band, redshifted relative to the monomer.[32]

1.1.4. Crystalline Anthracene

The excited-state properties observed in crystalline anthracene are quite different from those in solution. Both the absorption and emission spectrum of crystalline anthracene are redshifted relative to the solution spectrum and the fluorescence quantum yield is close to unity. The redshift in the spectra of crystalline anthracene indicates that the energy of the S_1 state is lowered. The discrepancy in Φ_F is attributed to the difference in the excited-state energies levels. In solution, the energies of the S_1 and T_2 state are 26,700 cm^{-1} and 14,850 cm^{-1} above the ground state, respectively. In crystalline anthracene, the T state energies do not change but the S_1 state is 25,440 cm^{-1} above the ground state. In solution, the $S_1 \rightarrow T_2$ energy gap is small and k_{ISC} competes with k_f, resulting in a lower Φ_F. However, in crystalline anthracene, k_{ISC} for the $S_1 \rightarrow T_1$ transition is large and does not compete with k_f, thus, $S_1 \rightarrow T_2$ is energetically unfavorable, and the Φ_F is high.[16]

1.2. Photophysics of Anthracene Derivatives

Numerous anthracene derivatives have been synthesized for a wide range of applications, which include organic light emitting diodes (OLEDs), photosensitizers and biological sensors.[33] Derivatization alters the excited-state properties of anthracene to varying degrees and is often used as a means to tune the optical properties for specific applications. Functionalization can shift the relative energies of the π-π* transitions, resulting in an increase in k_f and k_{ISC}. For example, the addition of methyl groups at the 9 and 10 positions of the center ring delocalizes electron density, shifting the energies of the singlet and triplet excited-state transitions. The energy of the lowest-lying singlet excited state (S_1) decreases and the energy of the triplet state (T) increases above that of S_1. Thus, ISC is no longer a competitive deactivation process and the fluorescence quantum yield is higher. When the methyl groups are replaced with phenyl groups, the energy of S_1 decreases even further while the T energy increases. As a result, the fluorescence quantum yield of 9,10-diphenylanthracene (9,10-DPA) is 0.95 and the quantum yield of the T state only ~ 0.04.[34]

Because of its high quantum yield of blue fluorescence, 9,10-DPA is often used as the TTA acceptor in upconversion systems. When coupled with $[\mathrm{Ru(dmb)_3}]^{2+}$, 9,10-DPA green-to-blue conversion was observed with upconversion efficiency approximately 24 times greater than that of anthracene under the same conditions.[31] The upconversion efficiency was further enhanced when the $[\mathrm{Ru(dmb)_3}]^{2+}$ donor was replaced with Pd(II)Octaethylporphyrin (PdOEP). 9,10-DPA and PdOEP (68:1) were embedded in a copolymer matrix and the resulting film was irradiated with 544 nm light to selectively excite PdOEP, and 9,10-DPA emission was observed. The UC emission was recorded under ambient conditions and showed a quartic (x^4) dependence on the incident light intensity. Furthermore, time-resolved experiments showed that PdOEP emission decay occurred with the same rate as growth in 9,10-DPA emission is generated.[35] This UC chromophore pair has also been employed in the assembly of soft material upconverting polymers using a polyurethane precursor. This polymerization method allows for precise control over the chromophore concentration and allowed the UC emission to be tuned to display blue, purple or red luminescence by varying the concentration of 9,10-DPA. These materials exhibited UC efficiencies >20%.[35]

9,10-DPA has also been studied for its use in organic light emitting diodes (OLEDs). Its wide-bandgap, high florescence quantum yield and bright blue emission make it a good candidate for OLEDs, however, 9,10-DPA can easily crystallize in the solid state, resulting in a nonhomogeneous films and increased resistance of the film, which limit performance of the device. The structure of 9,10-DPA selectively modifying to inhibit crystallization, the performance can be significantly enhanced, while maintaining the advantages of an anthracene-based materials. Shu *et al* developed OLEDs containing the anthracene derivatives 2-*tert*-butyl-9,10-bis[4′-(9-*p*-tolylfluoren-9-yl)biphenyl-4-yl]anthracene (BFAn) as the emitter and 2-*tert*-butyl-9,10-bis[4′-(1-phenylbenzoimidazyl)biphenyl-4-yl] (BIAn) as the electron transporter.[1b] The tert-butyl group disrupts the symmetry and inhibits crystallization while addition of the 9,9-fluorenyl substituents yields a deeper blue emission and affords steric hindrance that improve the overall structural stability.[36]

1.2.1. Aggregate Induced Emission (AIE)

Tian and coworkers reported a series of four 9,10-distyrylanthracene (DSA) derivatives that exhibited aggregate-induced emission (AIE).[37] These DSA derivatives exhibited weak, broad orange emission in solution, but in the crystalline state, display a bright green emission with a high fluorescence quantum yield. The low quantum yields observed in solution are attributed to fast nonradiative decay pathways through intramolecular torsion between 9,10-anthylene and the vinylene moiety. In the crystalline state, each DSA derivative is tightly packed into a nonplanar conformation due to intermolecular CH–π hydrogen bonding. Thus, torsional motions are restricted by the intermolecular interactions in the crystal, resulting in considerably increased fluorescence.[37] Similarly, 9,10-bis((E)-2-(pyrid-2-yl)vinyl)anthracene BP2VA also exhibits a weak orange emission (~ 583 nm) in dilute solution, while that of crystalline BP2VA is bright green (~ 528 nm). Additionally, piezoluminescence is observed in aggregates of BP2VA.[38] Grinding of the crystalline BP2VA powders results in a redshift of 33 nm in the emission spectrum. The emission at 528 nm can be gradually redshifted up to 561 nm with increasing external pressure. Furthermore, this process can be fully reversed by heating the powders to 160 ºC. To investigate the nature of this change in fluorescence, three crystal polymorphs of BP2VA were prepared with increasing π-π* interactions. As π-π* interactions in the crystal polymorphs increased, a redshift in the BP2VA emission spectrum was observed. Therefore, as external pressure increases, π-π* interactions are enhanced, resulting in the observed piezochromic effects. Thus, the redshift in the emission spectrum of BP2VA observed upon grinding the powders is attributed to increased exciton coupling and orbital overlap between chromophores in the crystal.[38] Reversible piezoluminescence has also been shown in solvated crystals of 9,10-Di(pyridin-4-yl)anthracene derivatives where the interchromophore distances were tuned by variation of the solvent, resulting in redshifted emission. Additionally, desolvated crystals displayed vapoluminescent behavior upon exposure to solvent vapors.[39]

Because of the unique photophysical properties of anthracene and its derivatives have been used as a building block in many supramolecular systems. Specifically, anthracene derivative that contain multiple carboxylic acid groups have been integrated into metal-organic frameworks (MOFs). The photophysics of anthracene derivatives can be fine-tuned through variation of the MOF structure in order to exploit the desired properties of anthracene within these materials. The following section will review the current research concerning anthracene-based MOFs and their photophysical properties.

1.3. Anthracene-based Luminescent Metal-Organic Frameworks

MOFs are crystalline materials composed of metal ions or metal clusters (nodes) connected by multi-dentate organic ligands (linkers) to form extended coordination networks. MOFs often have significant porosity and can also have relatively high chemical and thermal stability. Furthermore, their chemical and physical properties can be tuned by variation of the metal nodes or organic linkers. Often, the metal linkers contain conjugated aromatic ring systems that can produce luminescence. Luminescent MOFs (LMOFs) have been studied for their application in optoelectronics, dye-sensitized solar cells, photocatalysis, chemical sensing, bioimaging and drug delivery.[40,41] A number of anthracene derivatives have been incorporated into metal-organic frameworks (Figure 1.3.1). Early on, the majority of these MOFs were studied primarily for gas adsorption.[42,43,44] More recently, a number of anthracene-based MOFs have been synthesized and studied for their unique luminescent properties. Anthracene-based ligands contain multiple carboxylic acid groups, which coordinate to the metal ions to form M–O–C clusters, known as secondary building units (SBUs).[45] The SBUs provide the rigid joints of the framework, thus allowing for control of the MOF topology. Anthracene-based linkers have most commonly been incorporated into Zn^{2+} and Cd^{2+}–based MOFs, which can form square, tetrahedral or octahedral SBUs. Incorporation into MOFs with clusters of Zr^{4+} as the nodes affords greater stability, as the carboxylate groups bond more strongly since the Zr^{4+} ions are hard acids while the carboxylates are soft bases. Additionally, Zr^{4+} can form highly connected M–O–C clusters, which also increase the stability of the framework. For example, the recently reported Zr-MOF NNU-28 comprises $Zr_6O_4(OH)_4(CO_2)_{12}$ SBUs, which are coordinated to 12 anthracene-based ligands.[46] Anthracenic MOFs with Fe^{3+} and Ba^{2+} metal nodes have also been reported.[47,48]

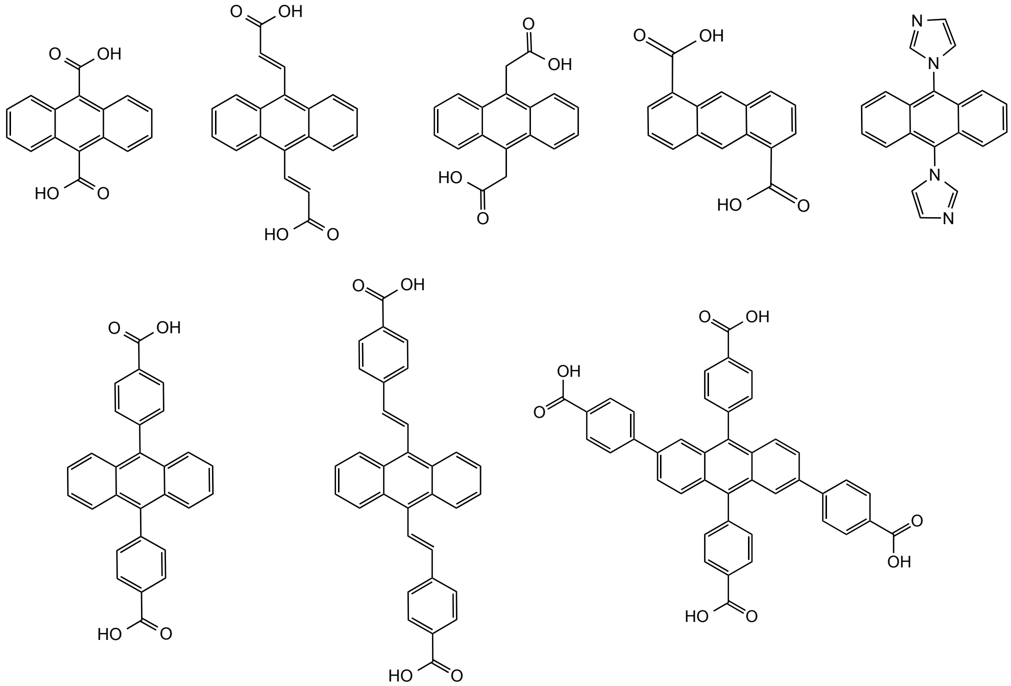

Figure 1.3.1. Molecular structures of the anthracene linkers that have been incorporated into luminescent MOFs.

1.3.1. Tuning the Topology and Functionality

Incorporation into a metal-organic framework alters the photophysical properties of the anthracene derivative. The rigid MOF structure can stabilize the chromophore, resulting in longer excited-state lifetimes and higher quantum yields due to reduction in non-radiative decay pathways. Excited-state properties of the linker can be further tuned based on the coordination environment within the MOF. For example, in one study, the anthracene derivative, 5,5′-(2,3,6,7-tetramethoxyanthracene-9,10-diyl)diisophthalic acid (H_4L^{OMe}) was incorporated into five different MOFs and resulted in different topologies.[49] The L^{OMe} linker adapts to coordinate to the different metals with various coordination geometries. By varying the metal ions and synthesis conditions, $[Mn_4(L^{OMe})(OAc)_2(\mu^3\text{-}OH)_2(NMP)_4(H_2O)_2]\cdot 2H_2O$, $[Ni_2(L^{OMe})_{0.5}(H_2L^{OMe})_{0.5}(\mu^3\text{-}OH)(H_2O)_3]\cdot 6H_2O$, $[Cd_2(L^{OMe})(H_2O)_2(NMP)]\cdot 2DMF\cdot NMP\cdot H_2O$, $[Co_2(L^{OMe})(H_2O)_3]\cdot 2NMP\cdot DMA\cdot$ H_2O, and $[Zn_2(L^{OMe})(H_2O)_2]\cdot 2NMP\cdot 2H_2O\cdot DOE$ were obtained. The manganese and nickel-based MOFs have planar tetranuclear secondary building units (SBUs) that form 2D sheets that form a 3D structure through π–π stacking. The cadmium metal ions form a 3D network and have a dinuclear SBU with the anthracene linker bridging two Cd metal ions. Both the cobalt and zinc MOFs crystallize into 3D networks and have analogous structures with three different types of coordination at the metal nodes. The solid-state luminescence of the Mn Cd and Zn-based based MOFs were measured and compared with that of the free ligand. “H_4L^{OMe} displays emission with a maximum at 467 nm (λ_{ex} = 270 nm), ascribed to the π*–π transitions of the parent anthracene ring system. All three MOFs display linker-based luminescence that is blueshifted relative to the free linker, with maxima at 444 nm (λ_{ex} = 270 nm), 442 nm (λ_{ex} = 290 nm) and 443 nm (λ_{ex} = 300 nm), for the Mn, Cd and Zn-based MOFs, respectively. The blueshift in the emission spectrum is attributed to stabilization of the excited state of the chromophore upon coordination in the MOF, which lowers the energy of the electronic transition.[49]

In some cases, the linker can be varied while still maintaining the crystal structure of the MOF. UiO-66 is a well-known isoreticular MOF (IRMOF) with a $Zr_6O_4(OH)_4$ SBU and 1,4-benzenedicarboxylate (BDC) linkers that form an octahedral cage geometry.[50–51] When BDC is replaced with 9,10-anthracenedicarboxylic acid (9,10-ADCA), the resulting framework is isostructural with UiO-66 but displays a redshift in the absorption spectrum from ~ 350 nm – 440, nm to ~ 350 nm – 540 nm. With a band gap of 2.47 eV, the UiO-type anthracene-based MOF is a strong oxidant and proved to be a decent photocatalyst for the degradation of methyl orange.[52]

1.3.2. Host-Guest Interactions

Variation of the organic linker is also an effective way to vary the pore-size and to control intermolecular interactions between linkers by tuning the interchromophore distances.[53,41] Larger pores can allow for adsorption of small molecules or "guest species" that may interact with the anthracene units and alter the florescence of the MOF.[40] Anthracene can interact with other aromatic molecules to form charge transfer (CT) complexes that exhibit different emission spectra. Tanka *et al* prepared nanoscale luminescent MOFs containing ADCA ligands that demonstrate host-guest charge transfer interactions between ADCA and adsorbed species, *N,N*-methylanaline (MA), *N,N*-dimethylanaline (DMA) and *N,N*-dimethyl-*p*-toludine (DMPT).[54] The as-synthesized MOF has the chemical structure $\{[Zn_2(adca)_2(dabco)](DMF)_{3.6}(MeOH)_{1.8}(H_2O)_{1.8}\}_n$, in which the ADCA ligands form 2D $\{[Zn^{II}(adca)]\}_n$ linear sheets that are connected by the dabco ligands in a manner analogous to pillars (Figure1.3.2 a). After solvent is removed from the pores, the cross section of the channels of the framework are 5.6 Å × 5.8 Å with an intermolecular distance of 3.75 Å between the 2D sheets. Adsorption of the guest molecules, MA, DMA or DMPT, resulted in a redshift in the emission spectrum of the MOF by approximately 80 nm, 110 nm and 120 nm, respectively, which appeared as a broad, structureless band (Figure1.3.2 b, d). These spectral changes are characteristic of exiplex formation between anthracene and DMA, which follows CT interactions between excited state anthracene and the acceptor molecule. The authors reported a Φ_F of < 0.01 for the desolvated MOF, which is extremely low in comparison to that of the free ligand (*vide infra*).

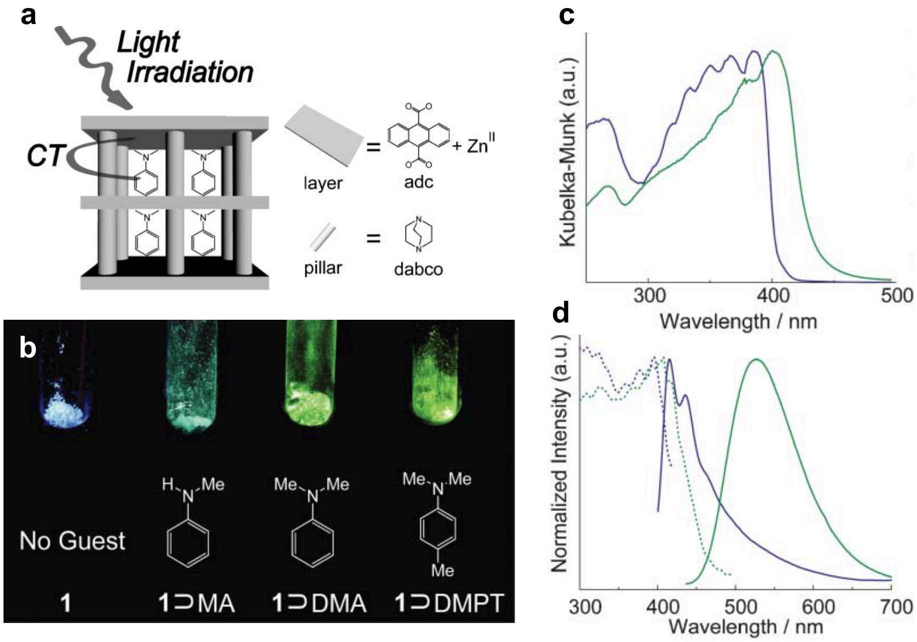

Figure1.3.2. (a) Scheme of host guest interactions in $\{[Zn_2(adca)_2(dabco)](DMF)_{3.6}(MeOH)_{1.8}(H_2O)_{1.8}\}_n$ (**1**) (b) Images of **1** with MA, DMA and DMPT samples under UV irradiation. (c) Diffuse reflectance spectra and (d) excitation (dotted line) and emission (solid line) spectra of **1** with MA (blue) and **1** with DMA (green). Images copied from reference 54.

Due to their porosity and high surface area, such materials have gained particular interest for their applications in chemical sensing, as they offer the potential for high uptake of analyte and enhanced sensitivity. Zang *et al* reported the self-assembled nanoscale LMOFs, containing 9,10-bis(4-carboxyphenyl)anthracene (BCPA) that demonstrated sensitive fluorescence detection of nitromethane and nitroaromatic explosive compounds. The fluorescence of the MOF is significantly quenched upon exposure to (dinitrotoluene) DNT or (trinitrotoluene) TNT vapors as a result of photoinduced electron transfer. When nitromethane was reduced to 1% saturated vapor with a concentration of 360 ppm, the fluorescence of the Zr-BPCA MOF was quenched by 21%. At 36,000 ppm and the fluorescence of the MOF is almost entirely quenched. On the other hand, fluorescence of the free BPCA linker is only quenched by 6% at 360 ppm and only 40% at 36,000 ppm. The enhanced quenching efficiency of BPCA was ascribed to the high surface area within the MOF and possibly, enhanced reducing ability of the nitro-compounds in the presence of Zn^{2+} ions.[55]

A MOF containing (2E,2′E)-3,3′-(anthracene-9,10-diyl)diacrylic acid connected to Cd^{2+} metal clusters was also explored for fluorescence detection of nitroaromatic compounds.[56] The MOF fluorescence was quenched in the presence of electron-deficient nitroaromatic molecules. In the presence of electron-rich aromatics the MOF exhibits a dual-response dependent upon the excitation wavelength; at 368 nm excitation, fluorescence quenching was observed, however, when excited at 200 nm, the fluorescence intensity increased by 20%. The nature of this dual-response was further investigated using density functional theory (DFT) calculations of the highest occupied molecular orbital (HOMO) and the lowest unoccupied molecular orbital (LUMO). These calculations revealed that the LUMO of the MOF is higher in energy than that of the electron-deficient nitroaromatics and lower than that of the electron-rich compounds. The different fluorescence responses were attributed to different charge transfer pathways. This anthracene-based MOF also exhibited chemiluminescence at 530 nm in the presence of peroxide.

Fluorescence detection of 4-nitrophenol (4-NP) as well as Al^{3+} and Fe^{3+} ions by a barium-MOF, $\{Ba_5(ADDA)_5(EtOH)_2(H_2O)_3{\cdot}5DMF\}_n$ (UPC-17; where DMF = N,N-dimethylformamide and ADDA = 3,3′-(anthracene-9,10-diyl)diacrylic acid), has also been demonstrated.[48] Upon incorporation into the framework, the ADDA emission spectrum was blueshifted 14 nm, from 560 nm to 546 nm. UPC-17 exhibited a solvent-dependent emission spectrum, which shifted from 495 nm in methanol to 535 nm in acetone and 552 nm in THF. When aliquots of a 4-NP solution were added to suspensions of 2 grams of UPC-17 in 3 mL of solvent, a steady decrease in the emission intensity was observed. Additionally, UPC-17 showed selective detection of 4-NP over other benzene derivatives. The addition of 233 μM 4-NP to UPC-17 suspended in acetone resulted in ~

80% quenching of the initial fluorescence intensity, 75% in THF and 60% in MeOH at the same 4-NP concentration. Fluorescence quenching was attributed to photoinduced electron-transfer from the ADDA ligand of UPC-17 to the analyte. UPC-17 also showed selective emission sensitivity to Fe^{3+} and Al^{3+} ions. In MeOH, the bright yellow-green fluorescence intensity decreased gradually with the addition of $Fe^{3+.}$ At 70 µL (233 µM), ~ 90% of the initial fluorescence intensity was quenched, However, in acetone, when 233 µM Fe^{3+} was added, the initial intensity of UPC-17 only decreased by 23%. Interestingly, in THF, the fluorescence intensity of UPC-17 increased with Fe^{3+} ion concentration and was ~ 4.5 times greater than the initial intensity and at 233 µM Fe^{3+}. Furthermore, the UPC-17 fluorescence shifted from bright yellow (~ 490 nm) to yellow-green (~ 510 nm) with the addition of Fe^{3+} ions. Similarly, the addition of an Al^{3+} solution resulted in enhanced fluorescence intensity up to ~8 times the initial intensity at 233 µM Al^{3+}. However, in contrast to Fe^{3+}, the addition of Al^{3+} to a UPC-17/MeOH suspension did not significantly alter the fluorescence. Fluorescence quenching by the metal ions was ascribed to interference of the metal ions with intraligand or ligand-to-ligand energy transfer processes with in the MOF.

1.3.3. Core-Shell MOFs

Core-shell MOFs (CS-MOFs) have been developed as a means of improving selectivity of MOFs designed for fluorescent sensing. Kitagawa *et al* prepared a CS-MOF with a $[Zn_2(bdc)_2(dabco)]_n$ (bdc = 1,4-benzene dicarboxylate , dabco = 1,4-diazabicyclo[2.2.2]octane) core and $\{Zn_2(adca)_2(dabco)\}_n$ shell.[57] Microscopic laser Raman spectroscopy (MLRS) was used to characterize the CS-MOF crystals, which were mechanically sliced at the middle of the crystal. A shell thickness of several tenths of a micrometer was determined by MLRS mapping and growth of the core and shell frameworks into one crystal confirmed by synchrotron X-ray diffraction measurements. ^{1}H NMR spectrum obtained after digestion of the CS-MOF crystals in HCl revealed a core-to-shell ratio of 8:2. The adsorption of petroleum molecules was explored using MLRS core, shell and CS-MOF crystals were soaked in either cetane or isocetane then filtered and dried. The Raman spectra of the crystals were then recorded at the core of the crystal and at the edge of the crystal (Figure 1.3.3). Raman spectra of the core MOF displayed characteristic signals of both cetane and isocetane, while only cetane was observed in the shell MOF. Raman spectra of the CS-MOF displayed only a cetane signal at the core of the CS-MOF, while no isocetane signal was observed in either the core or shell. The CS-MOF crystals were also soaked in a 1:1 mixture of cetane/isocetane then digested in HCl and the adsorption ratio was determined by gas chromatography mass spectroscopy (GCMS). The core crystals showed little discrimination between the isomers, while only cetane molecules accumulated in the shell crystals. Thus, the shell crystal can adsorb the cetane molecules but the bulkier isocetane molecules do not fit through the smaller pores, allowing for size-selective adsorption of guest molecules.

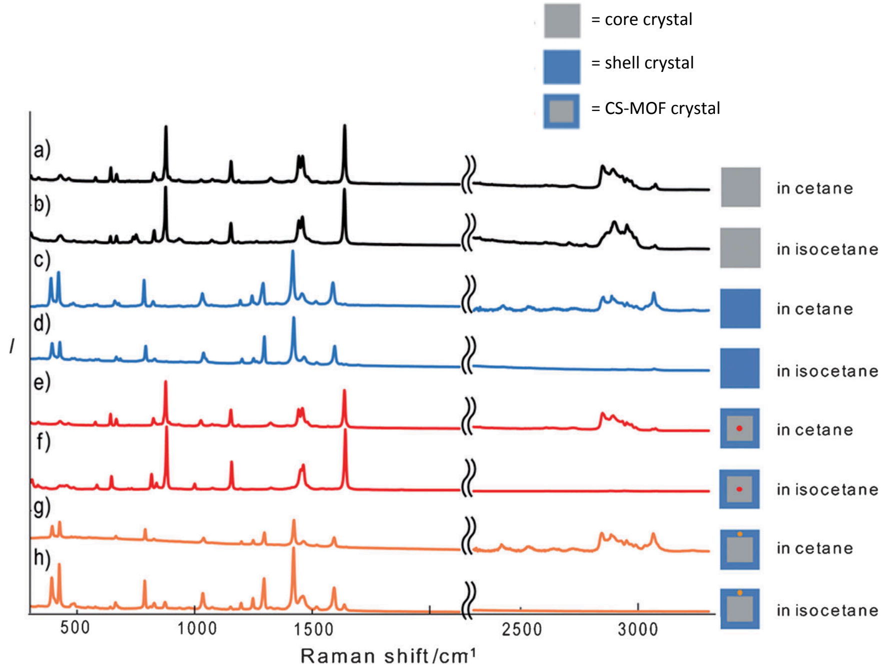

Figure 1.3.3: Raman spectra of single crystals of the core MOF after soaking in cetane (a) and isocetane (b), single crystals of the shell MOF after soaking in cetane (c) and (d) isocetane and the

core portion of the CS-MOF after soaking in cetane (e) and isocetane (f) and from the shell portion of the CS-MOF in cetane (g) and isocetane (h), the red and orange points in the CS-MOF crystal indicate the points where the Raman laser was focused. Figure modified from reference 57.

Kitagawa *et al* also reported CS-MOFs with the luminescent framework, $[Zn_2(adca)_2(dabco)]_n$ (**1**) as the core and $[Zn_2(bdc)_2(dabco)]_n$ (**2**) as the shell.[58] An amino group was introduced into the core of the CS-MOF (**1–2**) through post-synthetic modification (PSM) and replaced by a carboxyl group to increase the affinity for DMA over benzene, resulting in a CS-MOF with $[Zn_2(NH_2\text{-}bdc)_2(dabco)]_n$ as the core (**1–p2**, Figure 1.3.4 a). MOF **1** has shown fluorescence sensitivity to small aromatic molecules due to exciplex formation between the anthracene unit, which acts as an electron acceptor and DMA, the electron donor. Confocal light scanning microscopy (CLSM) was used to examine the fluorescence properties of **1**, **1–2** and **1–p2**. To test the selectivity of the CS-MOFs, fluorescence spectra were recorded in *N,N*-dimethylaniline (DMA), benzene and a 1:1 mixture of the two (Figure 1.3.4 b). The anthracene-based fluorescence of **1** and **1–2** at 420 nm was significantly quenched in DMA and a new broad emission band appeared in the 400 – 700 nm range. The broad emission is attributed to a photoinduced CT complex formation of an exciplex between the host anthracene unit and guest DMA molecules. The emission spectrum of **1** and **1–2** in the 1:1 mixture showed both the broad exciplex emission (400 – 700 nm) and monomeric anthracene emission at 420 nm. In contrast, the fluorescence spectrum of the **1–p2** in the solvent mixture showed predominantly exciplex fluorescence. Additionally, the maximum intensity of the exciplex emission of the core crystal is ~1.9 times stronger than that of **1** and **1–2**. Thus, the PSM CS-MOF improves detection of guest molecules shell through selective uptake of guest species, resulting in enhanced fluorescence-response from the core MOF.

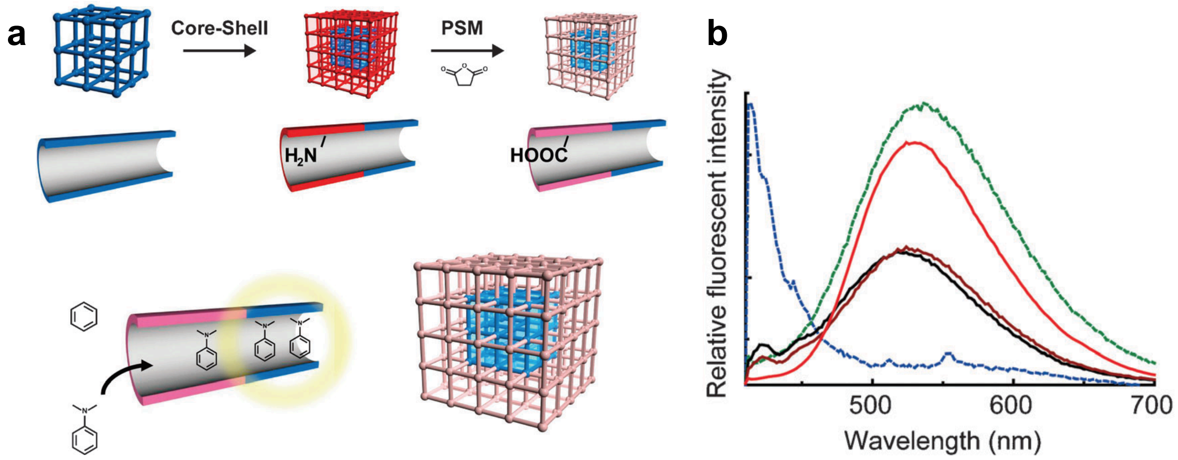

Figure 1.3.4: (a) Schematic illustration of core-shell MOF assembly and functionalization (b) CLSM fluorescence spectra of **1** in benzene (blue), **1** in DMA (green), **1** in 1:1 benzene/DMA mixture (black), **1–2** in the mixture (brown) and **1–p2** in the mixture (red), l_{ex} = 405 nm. Images from reference 58.

1.3.4. Photocatalysis

LMOFs offer excellent platforms for photocatalysis because of their chemical and thermal stability, high surface area and porosity as well as their ability for uptake and storage of small molecules. There have been several reports of catalytic CO_2 reduction using MOFs with Zr metal clusters as the catalytic site.[59,60] Recently, a Zr-based MOF containing 9,10-bis(4-carboxyphenyl)anthracene (9,10-BCPA) demonstrated high uptake of CO_2 (33.42 cm^3 g^{-1} at 298 K and 1 atm).[46] The NNU-28 MOF also displayed broad UV-vis absorption in the ~ 300 – 600 nm range (Figure 1.3.5 a). Broadening of the absorption band compared to that of the free linker was attributed to coordination of the photoactive ligand to the Zr SBU. Photoinduced charge generation of NNU-28 was then investigated using surface photovoltage (SPV) spectroscopy to measure change in surface voltage following UV-vis absorption. The SPV spectrum of NNU-28 correlated with that of the ligand (Figure 1.3.5 b), indicating that photoinduced charge generation in the MOF arises from visible light absorption by the ligand. The photocatalytic ability of NNU-28 was tested in the reduction of CO_2 to formate in the presence of TEOA as an electron and hydrogen donor to recycle the catalyst. Ion chromatography showed an increase in of $HCOO^-$ formate anion concentration over time under continuous visible-light illumination. The average formation rate of $HCOO^-$ was estimated to be 183.3 mmol h^{-1} $mmol_{MOF}^{-1}$. Control experiments performed in the dark or in the absence of NNU-28 showed no formate production. PXRD patterns of the NNU-28 MOFs indicated that crystal structure of the MOF was retained. Furthermore, NNU-28 could be reused up to three cycles with little decrease in photocatalytic activity. Control experiments using an equimolar amount of the free anthracene-based ligand in place of NNU-28 resulted in generation of 7.2 mmol formate anions within 10 hours under the same conditions. Thus, the anthracene-based ligand accounts for ~ 27% of CO_2 conversion in NNU-28. Additional control experiments, in which the reaction solution was pre-degassed by N_2 instead of CO_2, verified that the formate anion was a produced by CO_2 reduction only and not by ligand decomposition. To further investigate the mechanism of NNU-28 photocatalysis, electron paramagnetic resonance (EPR) studies were performed in the dark and light for both the free ligand and NNU-28 (Figure 1.3.5 c,d). An enhanced signal at $g = 2.003$ was observed in the light compared to the dark, indicating light-induced radical formation, which is responsible for CO_2 reduction by the free ligand. NNU-28 showed no EPR signal in the dark, while in the light, the signal at $g = 2.003$ was observed. Time-resolved experiments showed the signal intensities increased under continuous irradiation and reached the maximum at about 4 min and two additional signals appeared that were not observed in the ligand at $g = 2.009$ and 2.030. These two EPR signals were previously observed in the zirconium-based MOF, UiO-66 and were ascribed to sensitization of the Zr_6-oxo cluster through the LMCT process. All together, these experiments demonstrate that both the anthracene-based ligand and Zr_6-oxo cluster contribute to photocatalytic CO_2 reduction by NNU-28.

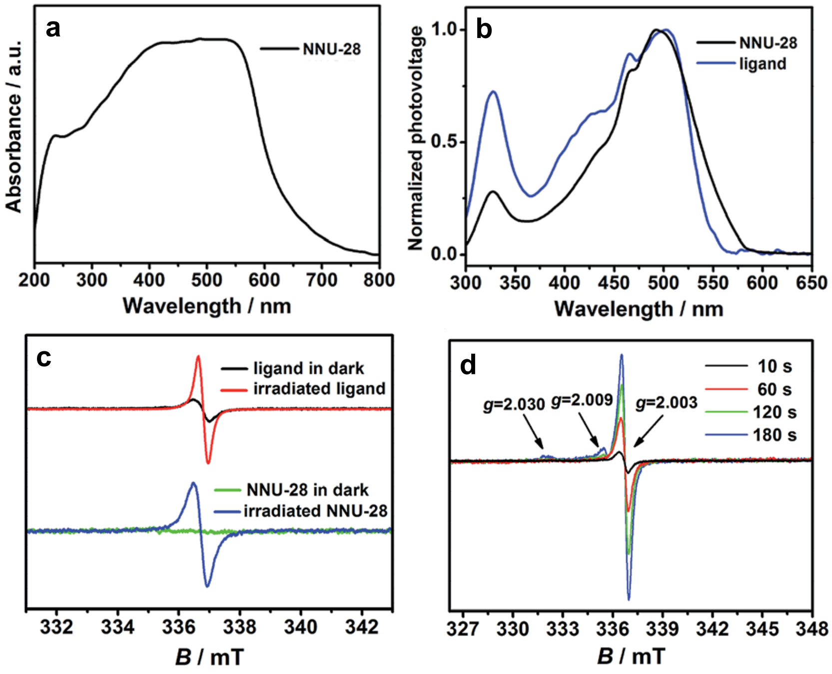

Figure 1.3.5. (a) UV-vis absorption spectrum of NNU-28 (b) SPV spectrum of NNU-28 (black) and the ligand (blue) (c) EPR signals of the ligand in the dark (black) and light (red) and NNU-28 in the dark (green) and light (blue) (d) time-evolution EPR signal of NNU-28 under continuous visible light illumination. Figures from reference 46.

LMOFs have also been employed in photoinduced polymerizations. Recently, the Zn-based MOF, NNU-35 with a pillar-layer structure comprising [9,10-bis(4′-pyridylethynyl)-anthracene] (BPEA) "layers" and BDC "pillars", was used as the photosensitizer in the copper catalyzed atom transfer radical polymerization (ATRP) of methacrylates. Photoinduced ATPR involves electron transfer from a photosensitizer to a Cu(II) catalyst, generating the Cu(I) catalyst, which activates alkyl halides by halogen transfer to form radicals. These radicals drive the polymerization until deactivated by the Cu (II) catalyst. NNU-35 has extremely broad UV-vis absorption spanning the 330 – 800 nm. The broadened absorption of NNU-35 was attributed to energy-transfer and charge-transfer interactions in the MOF. EPR studies reveal long-lived photoinduced charge separation in NNU-35, attributed to the free radical formation from the BPEA ligand. The ability of NNU-35 to mediate ATRP reactions was demonstrated in the polymerization of methacrylate monomers. NNU-35 photoinduced reaction polymerized 48% monomer after 8 h irradiation with a molecular weight distribution (M_w/M_n) of 1.12. Control experiments showed no polymerization occurred in the absence of NNU-35. The ability of NNU-35 to control photopolymerization by light switching was also shown. The proposed mechanism of NNU-35 mediated ATRP is shown in Figure 1.3.6, where the Cu(II) complex is reduced by NNU-35 by a 1 electron transfer, the resulting Cu(I) complex reacts alkyl halide (R–X) to form radicals (R•), which initiate the ATRP. The ligand radical of NNU-35 gains an electron from the reductive amine, returning to its original state, and the reaction intermediate ($amine^+X^-$) returns the chain-end halogen.

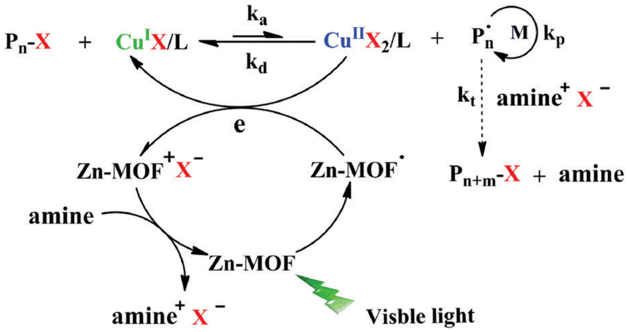

Figure 1.3.6: Proposed mechanism for NNU-35 photoinitiated ATRP.

1.3.5. Conductivity and Electroluminescence

The ability to tune the structure of MOF allows for control of interaction between anthracene units. A microporous Zn-MOF, NNU-27, was constructed from the anthracene-based, BPEA ligands, which formed zigzag chains with face-to-face distances of 3.420 Å through π-stacking between ligands. As a result of the distinct spatial arrangement of anthracene units in the MOF, NNU-27 exhibited both conductivity as well as electroluminescence. Current-voltage (I-V) measurements NNU-27 single crystals and the resulting I–V curves showed linear dependence at ambient temperature, revealing charge transport in the NNU-27 crystals. The conductivity of the

MOF was determined by measuring the effective contact area and was found to be 1.3 (±0.5) × 10^{-3} Scm^{-1}. NNU-27 also displayed orange-red electroluminescence emission, centered at 575 nm, under an applied voltage of ~ 27 V. The electroluminescence of NNU-27 arises from to the formation of electromers induced by the electric field.[61]

1.3.6. Scintillating MOFs

Scintillating materials display luminescence upon absorption of charged particles or high-energy radiation. Anthracene can be excited into higher singlet states upon absorption of ionizing radiation and subsequently undergo fast internal conversion to the lowest singlet excited state, from which fluorescence occurs. Crystalline anthracene displays the highest scintillation of (light output per unit energy) of any organic scintillator and is often used as a standard. However, the usefulness of anthracene crystals is limited by a number of drawbacks as they are fragile, quickly photo-oxidized in air and scintillation efficiency strongly depends on the temperature, degree of perfection and crystal thickness while large crystals are not easily obtained.[62]

Alledorf *et al* have explored a series of scintillating MOFs and have found that the stability of the scintillators to radiation damage is improved when incorporated into a MOF structure.[63] 5,5′-(anthracene-9,10-diyl)diisophthalic acid (DPATC) was incorporated into the Zn-based MOF, PCN-14-Zn and to study the effects of linker conjugation.[64] The MOF exhibited a similar emission spectrum to that of the free DPATC linker, however, the absorption spectrum was significantly blueshifted, indicating that there is a higher energy barrier for excitation in the MOF. DFT calculations revealed that rotation of the phenyl groups of DPATC occurs upon excitation from dihedral angles of 67.9° in the ground state to 56.8° and 54.9° in the singlet and triplet excited states, respectively. Furthermore, the torsional rotation of the phenyl groups relative to the anthracene moiety was reduced due to the rigidity of the multidentate ligand upon coordination within the MOF, where a dihedral angle of 70º was observed in the crystal structure of the MOF. This also resulted in a shorter fluorescence lifetime in the MOF (τ_1 ~ 1ns, τ_2 ~ 5ns) compared to solution (τ_1 ~ 7 ns, τ_2 ~ 8ns, τ_3 ~ 9 ns) due to increased efficiency of non-radiative deactivation pathways. PCN-14-Zn exhibited a prompted scintillation of 3 ns, between the τ_1 and τ_2 of fluorescence and with lower efficiency relative to other scintillation MOFs studied.[64]

In another study, Lin *et al* reported two X-ray scintillating MOFs with 9,10-bis(4-carboxyphenyl)anthracene (BCPA) as the linker and Hf or Zr as the metal node and X-ray absorber.[65] Typically, organic scintillators do not interaction with X-rays to produce luminescence thus; Hf^{4+} and Zr^{4+} were introduced as X-ray antenna. Hf^{4+} and Zr^{4+} metal ions eject outer-shell electrons upon the absorption of X-rays from 20 − 200 keV. These electrons can then interact with the anthracene-based linkers to generate luminescence. Accordingly, when the Hf-MOF and Zr-MOF were subjected to X-ray excitation, bright radioluminescence was observed.

1.3.7. Multiphoton Harvesting and Upconversion

LMOFs are promising candidates for light-harvesting materials owing to properties such as structural diversity, tunability of absorption and emission wavelengths, high surface area and energy transport abilities.[66,67] Multiple phonon harvesting was recently realized in an anthracene-based MOF.[68] Multiphoton harvesting is a process of photon upconversion in which two or more photons are absorbed simultaneously, promoting a molecule into an excited state. The subsequent relaxation of the excited-state results in the emission of a photon with frequency greater than that of the absorbed photons. The multiphoton harvesting MOF was constructed from the anthracene derivatives, *trans,trans*-9,10-bis(4-pyridylethenyl)anthracene (An2Py), and trans,trans-4,4′-stilbenedicarboxylic acid (H_2SDC) connecting zinc-oxide metal nodes. The resulting MOFs consisted of 4-fold interpenetrating networks, where the H_2SDC ligands form linear sheets, joined together by the An2Py pillar ligands. Both anthracene and peryline were introduced into the frameworks as Förster resonance energy transfer (FRET) acceptors to enhance the luminescence of the MOFs. The fluorescence quantum yield of An2Py increased when integrated into the MOF due to the structural rigidity and the emission spectrum resembled that of the anthracene derivative. The doped MOFs exhibited higher quantum yields than the undoped MOF. π–π stacking interactions between the guest anthracene or perylene molecules with the An2Py along with FRET from the guest species to the organic-linkers resulted in quenching of guest fluorescence concurrent with increased emission from the MOF. The MOFs have an absorption maximum at 400 nm, and displayed UC luminescence due to 2, 3 and 4 photon absorption upon excitation at 800 nm, 1200 nm and 1500 nm, respectively. Additionally, the UC luminescence showed a dependence upon excitation intensity. The development of materials for multiphoton upconversion is of interest in a variety of fields including biological imaging, photodynamic therapy, optical data storage and lasing.[68]

1.3.8. Triplet-Triplet Annihilation-Based Upconversion

Fluorescence upconversion through triplet-triplet annihilation (TTA) was also recently demonstrated in anthracene-based MOFs. TTA-based upconversion offers particular advantages in the field of solar energy harvesting where, in contrast to multi-photon absorption processes, TTA can be achieved using low-power, non-coherent excitation sources.[25] Three zinc-based MOFs containing the anthracene derivative, adb were explored, $[Zn_2(adb)_2(dabco)]_n$ (1) MOF and $[Zn_2(adb)_2(bpy)]_n$ (2) MOFs (where adb = 4,4′-(anthracene-9,10-diyl)dibenzoate and bpy = 5,5′-bipyridine) and $[Zn(adb)(DEF)_2]_n$ (3). The intermolecular distances between anthracene units (center-to-center) were 7.6 Å, 4.8 Å and 3.2 Å, for 1, 2 and 3, respectively. All three MOFs displayed upconverted emission when suspended in deaerated solutions of the TTA sensitizer, PdOEP, in benzene. Irradiation of the system with 532 nm light resulted in upconverted emission ~ 440 nm with TTET efficiencies of 12%, 8% and 59% for 1, 2 and 3, respectively. The emission showed a quartic dependence upon excitation intensity at lower intensities, indicative of TTA. PdOEP was modified with carboxyl groups and covalently attached to the surface of the nano-sized $[Zn(adb)(DEF)_2]_n$ MOFs. Under anaerobic conditions, these MOFs displayed upconverted blue fluorescence when excited with 532 nm light. To avoid overheating of the MOFs and photobleaching of PdOEP, the MOFs were encapsulated in PMMA. The TTET efficiency of the MOFs in these encapsulated PdOEP-modified MOFs was 61%. Additionally, the triplet lifetime of the MOF increased from 1 ms in benzene to 4 ms in PMMA, which was ascribed to further chromophore stabilization in the polymer matrix.[69]

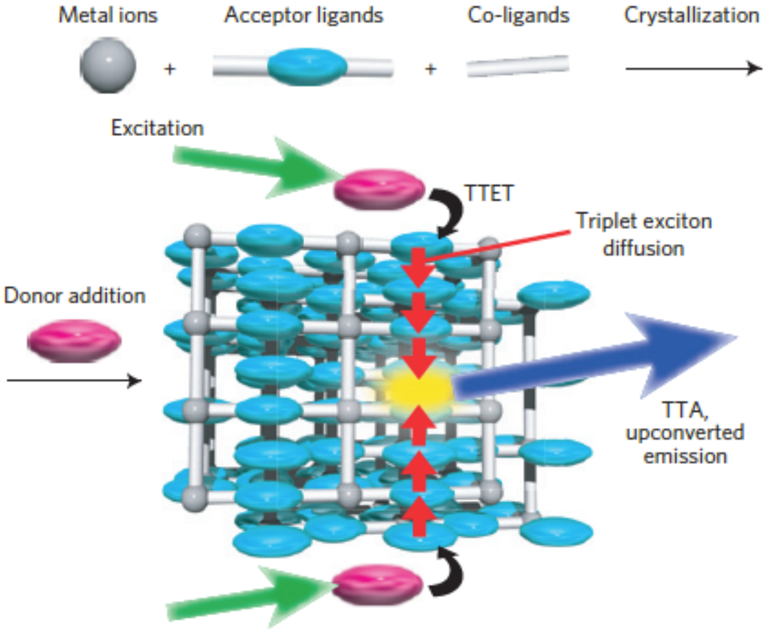

Figure 1.3.7: Schematic representation of excitation of TTET-donor molecules followed by TTET to the MOF and subsequent series of TTET, triplet exciton diffusion in the acceptor arrays and TTA between excited acceptor molecules, resulting in UC emission.[69]

1.4. Conclusions

The unique photophysical properties of anthracene have led to its widespread application in many fields. The excited-state properties of anthracene, such as the wavelength of emission, fluorescence lifetime and quantum yield, can be fine-tunes affording its broad versatility. Due to their distinct crystallinity, MOFs can afford an ideal material for studying specific interactions between anthracene ligands and/or interactions with guest species. A number of anthracene derivatives have been incorporated into MOFs for a variety of applications. The photophysical properties of the anthracene-based MOFs are generally related to that of the free anthracene-based ligand, however interactions can also be further modified when introduced into the crystalline framework through such as aggregate-induced emission, metal-to-ligand charge transfer, interactions with guest molecules that result in quenching or enhancement of fluorescence as well as interchromophore interactions such as π–π stacking.

1.5. Project Description

Anthracene-based MOFs have proved to be highly promising candidates in the development of photoactive materials with many avenues yet to be explored. In order to rationally design luminescent MOFs tailored for specific applications, a thorough understanding of the photophysical processes of the individual building blocks is essential. The goal of this project is to gain an understanding of the excited-state properties of the free organic linkers, including the effects of both derivatization and local environment and to then investigate how these properties are further altered upon incorporation into MOFs. To this end, three anthracene dicarboxylic acids (ADCAs) – 1,4-ADCA, 2,6-ADCA and 9,10-ADCA – were synthesized and their photophysical properties in solution were systematically studied. The organic linkers were then incorporated into zirconium-based MOFs and the excited state properties of the resulting MOFs were investigated.

1.6. References

1. (a) Becker, H. D., Unimolecular Photochemistry of Anthracenes. *Chem. Rev.* **1993,** *93*, 145–172; (b) Tao, S.; Xu, S.; Zhang, X., Efficient Blue Organic Light-Emitting Devices Based on Novel Anthracence Derivatives with Pronounced Thermal Stability and Excellent Film-Forming Property. *Chem. Phys. Lett.* **2006,** *429*, 622–627.
2. Zhu, M.; Yang, C., Blue Fluorescent Emitters: Design Tactics and Applications in Organic Light-Emitting Diodes. *Chem. Soc. Rev.* **2013,** *42*, 4963–4976.
3. Lackowicz, J. R., *Princeples of Fluorescence Spectroscopy 3rd Ed.* Springer Science+Business Media, LLC: 2010.
4. Valeur, B.; Berberan-Santos, M. N., *Molecular Fluorescence: Principles and Applications*. Wiley-VCH: 2012.
5. Platt, J. R., The Box Model and Electron Densities in Conjugated Systems. *The Journal of Chemical Physics* **1954,** *22* (8), 1448-1455.
6. Klevens, H. B.; Platt, J. R., Spectral Resemblances of Cata-Condensed Hydrocarbons. *The Journal of Chemical Physics* **1949,** *17* (5), 470-483.
7. Sidman, J. W., Electronic and Vibrational States of Anthracene. *J. Chem. Phys.* **1956,** *25*, 115-121.
8. Platt, J. R., Classification of Spectra of Cata-Condensed Hydrocarbons. *J. Chem Phys.* **1949,** *17*, 484-495.
9. Klevens, H. B.; Platt, J. R., Spectral Resemblances of Cata-Condensed Hydrocarbons. *The Journal of Chemical Physics* **1949,** *17* (5), 470-481.
10. Tigoianu, I. R.; Dorohoi, D. O.; Airinei, A., Solvent Influence on the Electronic Absorption Spectra of Anthracene. *Rev. Chim. (Bucharest, Rom.)* **2009,** *60* (1), 42-44.
11. Arnaut, L. G.; Formosinho, S. J., *Chemical Kinetics: From Molecular Structure to Chemical Reactivity*. Elsevier: Amsterdam, Boston, 2007.
12. Lakowicz, J. R., *Principles of Flourescence Spectroscopy*. Springer US: 2006.
13. Berlman, I. B., *Handbook of fluorescence spectra of aromatic molecules*. 2d ed.; Academic Press: New York,, 1971; p xiv, 473 p.
14. (a) Melhuish, W. H., Quantum Efficiencies of Fluorescence of Organic Substances: Effect of Solvent and Concentration of the Fluorescent Solute. *The Journal of Physical Chemistry* **1961,** *65* (2), 229-235; (b) Ware, W. R.; Baldwin, B. A., Absorption Intensity and Fluorescence Lifetimes of Molecules. *The Journal of Chemical Physics* **1964,** *40* (6), 1703-1705; (c) Dawson, W. R.; Windsor, M. W., Fluorescence yields of aromatic compounds. *The Journal of Physical Chemistry* **1968,** *72* (9), 3251-3260; (d) Lampert, R. A.; Chewter, L. A.; Phillips, D.; O'Connor, D. V.; Roberts, A. J.; Meech, S. R., Standards for Nanosecond Fluorescence Decay Time Measurements. *Analytical Chemistry* **1983,** *55* (1), 68-73.
15. Melhuish, W. H.; Hardwick, R., Lifetime of the Triplet State of Anthracene in Lucite. *J. Chem. Soc. Faraday Trans.* **1962,** *58*, 1908–1911.
16. Berlman, I. B., *Handbook of Fluorescence Spectra of Aromatic Molecules*. Academic Press: New York, 1971.
17. Pedash, Y. F.; Prezhdo, O. V.; Kotelevshiy, S. I.; Prezhdo, V. V., Spin–Orbit Coupling and Lumincescence Characteristics of Conjugated Organic Molecules. I. Polyacenes. *Journal of Molecular Structure (Theochem)* **2002,** *585*, 49-59.
18. Reineke, S.; Baldo, M. A., Room Temperature Triplet State Spectroscopy of Organic Semiconductors. *Scientific Reports* **2014,** *4*, 3797.

19. Shockley, W.; Queisser, H. J., Detailed Balance Limit of Efficiency of p‐n Junction Solar Cells. *Journal of Applied Physics* **1961,** *32*, 510-519.

20. Nichols, V. M.; Rodriguez, M. T.; Piland, G. B.; Tham, F.; Nesterov, V. N.; Youngblood, W. J.; Bardeen, C. J., Assessing the Potential of Peropyrene as a Singlet Fission Material: Photophysical Properties in Solution and the Solid State. *The Journal of Physical Chemistry C* **2013,** (117), 16802-16810.

21. Congreve, D. N.; Lee, J.; Thompson, N. J.; Hontz, E.; Yost, S. R.; Reusswig, P. D.; Bahlke, M. E.; Reineke, S.; Voorhis, T. V.; Baldo, M. A., External Quantum Efficiency Above 100% in a Singlet-Exciton-Fission–Based Organic Photovoltaic Cell. *Science* **2013,** *340*, 334-337.

22. Smith, M. B.; Michl, J., Singlet fission. *Chem. Rev.* **2010,** *110*, 6891–6936.

23. Burdett, J. J.; Bardeen, C. J., The Dynamics of Singlet Fission in Crystalline Tetracene and Covalent Analogs. *Accounts of Chemical Research* **2012,** *46* (6), 1312-1320.

24. Piland, G. B.; Bardeen, C. J., How Morphology Affects Singlet Fission in Crystalline Tetracene. . *J. Phys. Chem. Lett.* **2015,** *6*, 1841− 1846.

25. Zhou, J.; Liu, Q.; Feng, W.; Sun, Y.; Li, F., Upconversion Luminescent Materials: Advances and Applications. *Chem. Rev.* **2015,** *115*, 395–465.

26. Islangulov, R. R.; Kozlov, D. V.; Castellano, F. N., Low power Upconversion Using MLCT Sensitizers. *Chem. Commun.* **2005**, 3776–3778.

27. Singh-Rachford, T. N.; Castellano, F. N., Photon Upconversion Based on Sensitized Triplet–Triplet Annihilation. *Coordination Chemistry Reviews* **2010,** *254*, 2560-2573.

28. Kozlov, D. V.; Castellano, F. N., Anti-Stokes Delayed Fluorescence from Metal–Organic Bichromophores. *Chem. Commun.* **2004,** *2860* (24), 2860–2861.

29. Barber, R. A.; Mayo, P. d.; Okada, K.; Wong, S. K., Photosensitized [4 + 4'] Cycloreversion of Anthracene Dimer Via an Electron-Transfer Mechanism. *J. Am. Chem. Soc.* **1982,** *104* (18), 4995–4997.

30. Charlton, J. L.; Dabestani, R.; Saltiel, J., Adsorption of Bifunctional Organic Disulfides on Gold Surfaces. *J. Am. Chem. Soc.* **1983,** *105* (13), 4481–4483.

31. Islangulov, R. R.; Castellano, F. N., Photochemical Upconversion: Anthracene Dimerization Sensitized to Visible Light by a Ru(II) Chromophore. *Angew. Chem. Int. Ed.* **2006,** *45*, 5957–5959.

32. Birks, J. B.; Aldekomo, J. B., The Photodimerization and Excimer Fluorescence of 9-methyl Anthracene. *Photochem Photobiol* **1963,** *2*, 415–418.

33. (a) Shah, B. K.; Neckers, D. C.; Shi, J.; Forsythe, E. W.; Morton, D., Photophysical properties of anthanthrene-based tunable blue emitters. *J. Phys. Chem. A* **2005,** *109*, 7677–7681; (b) Moorthy, J. N.; Venkatakrishnan, P.; Natarajan, P.; Huang, D. F.; Chow, T. J., De Novo Design for Functional Amorphous Materials: Synthesis and Thermal and Light-Emitting Properties of Twisted Anthracene-Functionalized Bimesitylenes. *J. Am. Chem. Soc.* **2008,** *130* (51), 17320–17333; (c) Swager, T. M.; Gil, C. J.; Wrighton, M. S., Fluorescence Studies of Poly(p-phenyleneethynylene)s: The Effect of Anthracene Substitution. *J. Phys. Chem.* **1995,** *99* (14), 4886–4893.

34. Malkin, J., *Photophysical and Photochemical Properties of Aromatic Compounds*. CRC: Boca Raton, 1992.

35. Islangulov, R. R.; Lott, J.; Weder, C.; Castellano, F. N., Noncoherent Low-Power Upconversion in Solid Polymer Films. *J. Am. Chem. Soc.* **2007,** *129*, 12652–12653.

36. Raghunath, P.; Reddy, M. A.; Gouri, C.; Bhanuprakash, K.; Rao, V. J., Electronic Properties of Anthracene Derivatives for Blue Light Emitting Electroluminescent Layers in

Organic Light Emitting Diodes: A Density Functional Theory Study. *J. Phys. Chem. A* **2006,** *110* (3), 1152–1162.

37. He, J.; Xu, B.; Chen, F.; Xia, H.; Li, K.; Ye, L.; Tian, W., Aggregation-Induced Emission in the Crystals of 9,10-distyrylanthracened Derivatives: The Essential Role of Restricted Intramolecular Torsion. *J. Phys. Chem. C* **2009,** *113*, 9892–9899.

38. Dong, Y.; Xu, B.; Zhang, J.; Tan, X.; Wang, L.; Chen, J.; Lv, H.; Wen, S.; Li, B.; Ye, L.; Zou, B.; Tian, W., Piezochromic Luminescence Based on the Molecular Aggregation of 9,10-Bis((E)-2-(pyrid-2-yl)vinyl)Anthracene. *Angew. Chem.* **2012,** *124*, 10940–10943.

39. Kohmoto, S.; Chuko, R.; Hisamatsu, S.; Okuda, Y.; Masu, H.; Takahashi, M.; Kishikawa, K., Piezoluminescence and Liquid Crystallinity of 4,4′-(9,10-anthracenediyl)bispyridinium Salts. *Cryst. Growth Des.* **2015,** *15*, 2723–2731.

40. Allendorf, M. D.; Bauer, C. A.; Bhaktaa, R. K.; Houka, R. J. T., Luminescent Metal–Organic Frameworks. *Chem. Soc. Rev.* **2009,** *38*, 1330–1352.

41. Hu, Z.; Deibert, B. J.; Li, J., Luminescent Metal–Organic Frameworks for Chemical Sensing and Explosive Detection. *Chem. Soc. Rev.* **2014,** *43*, 5815–5840.

42. Ma, S.; Wang, X.-S.; Collier, C. D.; Manis, E. S.; Zhou, H.-C., Ultramicroporous Metal-Organic Framework Based on 9,10-Anthracenedicarboxylate for Selective Gas Adsorption. *Inorg. Chem.* **2007,** *46* (21), 8499–8501.

43. Ma, S.; Simmons, J. M.; Sun, D.; Yuan, D.; Zhou, H.-C., Porous Metal-Organic Frameworks Based on an Anthracene Derivative: Syntheses, Structure Analysis, and Hydrogen Sorption Studies. *Inorg. Chem.* **2009,** *48*, 5263–5268.

44. Ma, S.; Sun, D.; Forster, P. M.; Yuan, D.; Zhuang, W.; Chen, Y.-S.; Parise, J. B.; Zhou, H.-C., A Three-Dimensional Porous Metal-Organic Framework Constructed from Two-Dimensional Sheets via Interdigitation Exhibiting Dynamic Features. *Inorg. Chem.* **2009,** *48* (11), 4616–4618.

45. Kim, J.; Chen, B.; Reineke, T. M.; Li, H.; Eddaoudi, M.; Moler, D. B.; O′Keeffe, M.; Yaghi, O. M., Assembly of Metal-Organic Frameworks from Large Organic and Inorganic Secondary Building Units: New Examples and Simplifying Principles for Complex Ctructures. *J. Am. Chem. Soc.* **2001,** *123* (34), 8239–8247.

46. Chen, D.; Xing, H.; Wang, C.; Su, Z., Highly Efficient Visible-Light-Driven CO2 Reduction to Formate by a New Anthracene-Based Zirconium MOF via Dual Catalytic Routes. *J. Mater. Chem. A* **2016,** *4*, 2657–2662.

47. Vinogradov, A. V.; Milichko, V. A.; Zaake-Hertling, H.; Aleksovska, A.; Gruschinski, S.; Schmorl, S.; Kersting, B.; Zolnhofer, E. M.; Sutter, J.; Meyer, K.; Lönnecke, P.; Hey-Hawkins, E., Unique Anisotropic Optical Properties of a Highly Stable Metal–Organic Framework Based on Trinuclear Iron(III) Secondary Building Units Linked by Tetracarboxylic Linkers with an Anthracene Core. *Dalton Trans.* **2016,** (Advanced Article).

48. Wang, R.; Liu, X.; Huang, A.; Wang, W.; Xiao, Z.; Zhang, L.; Dai, F.; Sun, D., Unprecedented Solvent-Dependent Sensitivities in Highly Efficient Detection of Metal Ions and Nitroaromatic Compounds by a Fluorescent Barium Metal-Organic Framework. *Inorg. Chem.* **2016,** *55* (4), 1782−1787.

49. Liu, F.; Zhang, L.; Wang, R.; Sun, J.; Yang, J.; Chen, Z.; Wang, X.; Sun, D., Five MOFs with different topologies based onanthracene functionalized tetracarboxylic acid: syntheses, structures, and properties. *Cryst. Eng. Comm.* **2013,** *16*, 2917–2928.

50. Cavka, J. H.; Jakobsen, S.; Olsbye, U.; Guillou, N.; Lamberti, C.; Bordiga, S.; Lillerud, K. P., A New Zirconium Inorganic Building Brick Forming Metal-Organic Frameworks with Exceptional Stability. *J. Am. Chem. Soc.* **2008,** *130* (42), 13850–13851.

51. Katz, M. J.; Brown, Z. J.; Y. J. Colón, b.; Siu, P. W.; Scheidt, K. A.; Snurr, R. Q.; Huppa, J. T.; Farhaa, O. K., A Facile Synthesis of UiO-66, UiO-67 and Their Derivatives. *Chem. Commun.* **2013,** *49*, 9449–9451.

52. Pu, S.; Xu, L.; Sun, L.; Du, H., Tuning the Optical Properties of the Zirconium–UiO-66 Metal–Organic Framework for Photocatalytic Degradation of Methyl Orange. *Inorg. Chem. Comm.* **2015,** *52*, 50–52.

53. Banerjee, R.; Furukawa, H.; Britt, D.; Knobler, C.; O'Keeffe, M.; Yaghi, O. M., Control of Pore Size and Functionality in Isoreticular Seolitic Imidazolate Frameworks and Their Carbon Dioxide Selective Capture Properties. *J. Am. Chem. Soc.* **2009,** *131* (11), 3875–3877.

54. Tanaka, D.; Horike, S.; Kitagawa, S.; Ohba, M.; Hasegawa, M.; Ozawac, Y.; Toriumi, K., Anthracene Array-Type Porous Coordination Polymer with Host–Guest Charge Transfer Interactions in Excited States. *Chem. Commun.* **2007**, 3142–3144.

55. Zhang, C.; Che, Y.; Zhang, Z.; Yang, X.; Zang, L., Fluorescent nanoscale zinc(II)-carboxylate coordination polymers for explosive sensing. *Chem. Commun.* **2011,** *47*, 2336–2338.

56. Yang, X.-L.; Chen, X.; Hou, G.-H.; Guan, R.-F.; Shao, R.; Xie, M.-H., A Multiresponsive Metal-Organic Framework: Direct Chemiluminescence, Photoluminescence, and Dual Tunable Sensing Applications. *Adv. Funct. Mater.* **2016,** *26*, 393–398.

57. Hirai, K.; Furukawa, S.; Kondo, M.; Uehara, H.; Sakata, O.; Kitagawa, S., Sequential Functionalization of Porous Coordination Polymer Crystals. *Angew. Chem. Int. Ed.* **2011,** *50*, 8057–8061.

58. Hirai, K.; Furukawa, S.; Kondo, M.; Meilikhov, M.; Sakata, Y.; Sakata, O.; Kitagawa, S., Targeted functionalisation of a hierarchically-structured Porous Coordination Polymer Crystal Enhances its Entire Function. *Chem Commun (Camb)* **2012,** *48* (52), 6472-4.

59. Xu, H. Q.; Hu, J.; Wang, D.; Li, Z.; Zhang, Q.; Luo, Y.; Yu, S. H.; Jiang, H. L., Visible-Light Photoreduction of CO2 in a Metal-Organic Framework: Boosting Electron-Hole Separation via Electron Trap States. *J Am Chem Soc* **2015,** *137* (42), 13440-3.

60. Wang, G.; Sun, Q.; Liu, Y.; Huang, B.; Dai, Y.; Zhang, X.; Qin, X., A Bismuth-Based Metal-Organic Framework as an Efficient Visible-Light-Driven Photocatalyst. *Chemistry* **2015,** *21* (6), 2364-7.

61. Borges, D. D.; Devautour-Vinot, S.; Jobic, H.; Ollivier, J.; Nouar, F.; Semino, R.; Devic, T.; Serre, C.; Paesani, F.; Maurin, G., Proton Transport in a Highly Conductive Porous Zirconium-Based Metal-Organic Framework: Molecular Insight. *Angew Chem Int Ed Engl* **2016,** *55* (12), 3919-24.

62. Knoll, G. F., *Radiation detection and measurement*. 2nd ed.; Wiley: New York, 1989; p xix, 754 p.

63. Doty, F. P.; Bauer, C. A.; Skulan, A. J.; Grant, P. G.; Allendorf, M. D., Scintillating Metal-Organic Frameworks: A New Class of Radiation Detection Materials. *Adv. Mater* **2009,** *21*, 95–101.

64. Perry, J. J.; Feng, P. L.; Meek, S. T.; Leong, K.; Doty, F. P.; Allendorf, M. D., Connecting Structure with Function in Metal–Organic Frameworks to Design Novel Photo- and Radioluminescent materials. *J. Mater. Chem.* **2012,** *22*, 10235–10248.

65. Wang, C.; Volotskova, O.; Lu, K.; Ahmad, M.; Sun, C.; Xing, L.; Lin, W., Synergistic Assembly of Heavy Metal Clusters and Luminescent Organic Bridging Ligands in Metal−Organic Frameworks for Highly Efficient X-ray Scintillation. *J. Am. Chem. Soc.* **2014,** *136*, 6171–6174.

66. So, M. C.; Wiederrecht, G. P.; Mondloch, J. E.; Hupp, J. T.; Farha, O. K., Metal-Organic Framework Materials for Light-Harvesting and Energy Transfer. *Chem Commun (Camb)* **2015,** *51* (17), 3501-10.

67. Kent, C. A.; Mehl, B. P.; Ma, L.; Papanikolas, J. M.; Meyer, T. J.; Lin, W., Energy Transfer Dynamics in Metal-Organic Frameworks. *J Am Chem Soc* **2010,** *132* (37), 12767-9.

68. Quah, H. S.; Chen, W.; Schreyer, M. K.; Yang, H.; Wong, M. W.; Ji, W.; Vittal, J. J., Multiphoton harvesting metal–organic frameworks. *Nature Comm.* **2015,** *6*, 7954.

69. Mahato, P.; Monguzzi, A.; Yanai, N.; Yamada, T.; Kimizuka, N., Fast and Long-Range Triplet Exciton Diffusion in Metal–Organic Frameworks for Photon Upconversion at Ultralow Excitation Power. *Nat. Mater.* **2015,** *14*, 924–930.

2. Systematic Investigation of the Excited-State Properties of Anthracene-Dicarboxylic Acids

2.1. Introduction

Organic photoactive molecules are of interest due to the tunability and environmental susceptibility of their excited-state properties, which affords a range of optoelectronic applications including organic light-emitting diodes (OLEDs), photovoltaic cells, organic field effect transistors, and fluorescent sensing elements.[1,2,3,4] Anthracene is a polyaromatic hydrocarbon whose excited-state properties have been extensively studied.[5] Due to its unique ground and excited-state properties, anthracene and its derivatives are often incorporated into devices such as OLEDs and organic semiconductor materials for numerous applications.[6-9] However, in order to rationally tailor anthracene derivatives for a given application, an understanding of the effects of microenvironment and functionalization on the photophysical properties is essential.

The excited-state behavior of a carboxylic acid functionalized anthracene, 9-anthracenecarboxylic acid (9-ACA) has been the topic of a number of reports.[21-27] Changes in the emission spectra of 9-ACA have been argued to arise from acid-base equilibrium, solvent and concentration dependent dimerization and formation of higher order aggregates,[22,24] as well as structural reorganization[26] of the carboxylic acid relative to the anthracene ring in the excited state. In order to contribute to this discussion, we prepared a series of anthracene derivatives functionalized symmetrically with carboxylic acids; namely 2,6-anthracenedicarboxylic acid (2,6-ADCA), 1,4-anthracenedicarboxylic acid (1,4-ADCA), and 9,10-anthracenedicarboxylic acid (9,10-ADCA). We characterize the effect of functionalization on the energetics of the ground and excited states of anthracene using steady-state absorption and emission spectroscopies, emission lifetime measurements, density functional theory (DFT) and time-dependent DFT (TDDFT) calculations. The results are interpreted in light of structural/conformational differences between the ground and excited states of each anthracene derivative.

2.2. Results

The steady-state absorption and emission spectra of 2,6-ADCA (a,b), 1,4-ADCA (c,d) and 9,10-ADCA (e,f) measured in THF are shown in Figure 2.2.2. 2,6-ADCA displays vibronically structured absorption and emission bands. Although the structure of the emission spectrum closely resembles that of anthracene, the absorption spectrum differs from anthracene in both the number of lower-energy (~320 nm – 420 nm for 2,6-ADCA and 285 nm – 385 nm for anthracene) absorption bands and their intensities. The absorption spectrum of 1,4-ADCA appears broad with subtle structural features at 360 nm and 370 nm and the emission spectrum is broad and structureless. 9,10-ADCA exhibits vibronically structured absorption band, similar in shape to anthracene, while the emission spectrum is broad and diffuse. Both the absorption and emission spectra of each derivative are bathochromically shifted relative to anthracene. Additionally, the $^1A \rightarrow {}^1B_b$ absorption peak of 1,4-ADCA at 240 nm is significantly broadened and relative to anthracene and is split into two peaks. 2,6-ADCA exhibits a Stokes shift (584 cm^{-1} in THF) that is slightly larger than that of anthracene (277 cm^{-1} in THF). 1,4-ADCA and 9,10-ADCA display large Stokes shifts (4,803 cm^{-1} and 3,796 cm^{-1} in THF) compared to anthracene. The observed lifetimes of each isomer in THF are considerably longer than the 4.9 ± 0.1 ns fluorescence lifetime of anthracene in the same solvent (Table 2.2).

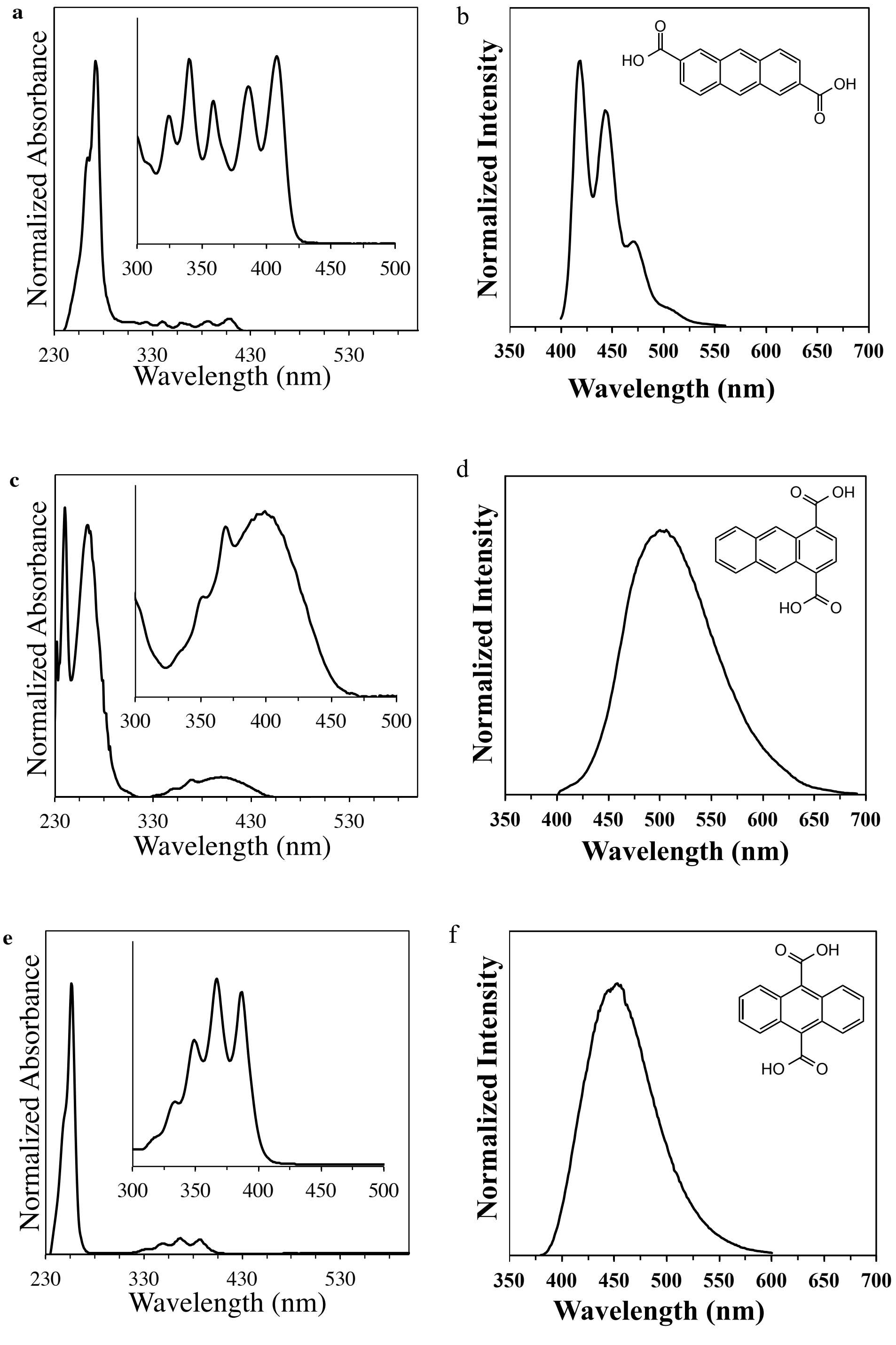

Figure 2.2.1. Absorption and emission spectra of 2,6-ADCA (a,b) 1,4-ADCA (c,d) and 9,10-ADCA (e,f).

In order to probe the effects of solvent polarity on the photophysical properties of the anthracene derivatives, the absorption and emission spectra as well as the lifetimes and quantum yields were measured in a series of polar aprotic solvents. Neither the absorption nor emission spectra of 9,10-ADCA are affected by solvent polarity. The absorption spectrum of 9,10-ADCA displays anthracene-like vibrational structure in all neat solvents tested. The emission spectrum is broad and diffuse with a λ_{max}^{em} around 455 nm in neat solvents, with the exception of 1,2-DCE, in which λ_{max}^{em} is bathochromically shifted by 14 nm (Figure S2.1, Table S2.1). The observed Stokes shift is 3,796 cm^{-1} ± 114 in THF, ethyl acetate, butanone, acetone and DMA, but larger in 1,2-DCE (4,521 cm^{-1}, Table S2.1). Similarly, solvent polarity has no significant effect on the absorption or emission spectra 2,6-ADCA, as the maxima do not shift significantly between THF ($\varepsilon = 7$, $\lambda_{max}^{abs} = 409$ nm, $\lambda_{max}^{em} = 419$ nm), and DMA ($\varepsilon = 38$, $\lambda_{max}^{abs} = 408$ nm, $\lambda_{max}^{em} = 421$ nm, Figure S2.2, Table S2.1). In contrast to the other two isomers, the absorption band of 1,4-ADCA is hypsochromically shifted by 10 nm, from 396 nm in THF ($\varepsilon = 7$) to 386 nm for DMA ($\varepsilon = 38$, Figure S2.3, Table S2.1), and the emission maximum is bathochromically shifted by 8 nm from 489 nm in THF to 497 nm in DMA. The absorption and emission spectra of 1,4-ADCA remain broad and diffuse in all of the neat solvents explored.

The fluorescence quantum yields (Φ_{fl}) and fluorescence lifetimes (τ_{fl}) along with the experimental radiative ($k_{r,exp}$) and non-radiative (k_{nr}) rate constants and calculated ($k_{r,calc}$) rate constant obtained from the Strickler-Berg equation for the three ADCA derivatives in the various solvents are listed in Table 2.2 and Table S2.2. No trends are observed between solvent polarity and fluorescence quantum yields over the solvent series (Table S2.2). In general, the fluorescence lifetimes are largely independent of solvent polarity but are considerably shorter in basic conditions.[17-20]

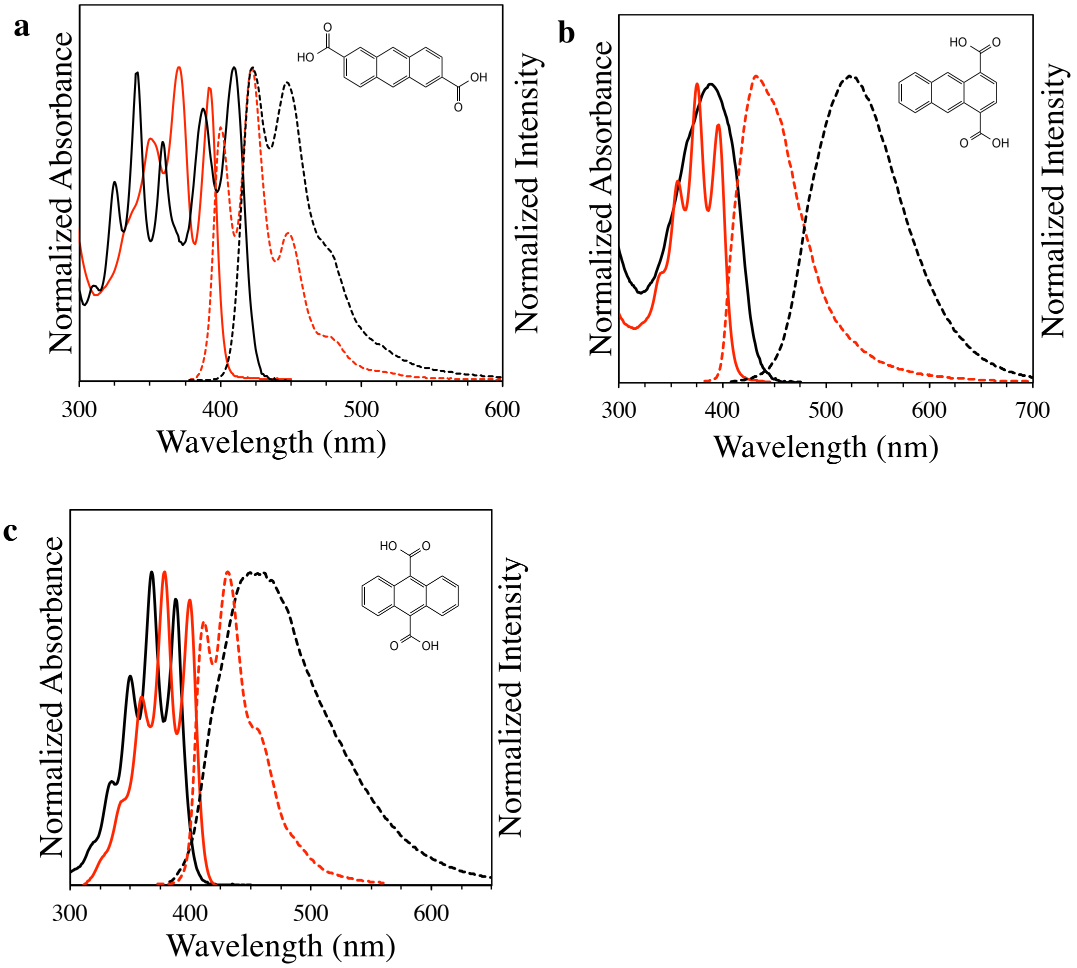

Figure 2.2.2. Absorption and emission spectra of 2,6-ADCA (a), 1,4-ADCA (b) and 9,10-ADCA (c) acidic DMF (black) and basic DMF (red).

To further explore how the protonation state of the carboxylic acid substituents affects the excited-state properties of the anthracene derivatives, photophysical measurements were carried out in acidic DMF and basic DMF (Figure 2.2.2, Table 2.2). All three isomers exhibit anthracene-like vibronic structure in the absorption spectra recorded in basic DMF. The emission spectrum of 2,6-ADCA displays more defined vibronic structure in basic solution compared to acidic. The emission spectrum of 1,4-ADCA remains broad and structureless in both basic and acidic environments. On the other hand, 9,10-ADCA exhibits a broad, diffuse emission spectrum in acidic DMF, but in basic DMF anthracenic vibronic structure is observed. The absorption spectra of 1,4-ADCA and 9,10-ADCA are hypsochromically shifted in basic DMF relative to acidic, while that of 2,6-ADCA is bathochromically shifted in basic solution. Additionally, the emission spectrum of each of the derivatives is hypsochromically shifted under basic conditions compared to acidic. The Stokes shifts decrease considerably with solvent pH, going from 948 cm^{-1} to 510 cm^{-1} for 2,6-ADCA, 6,484 cm^{-1} to 1,997 cm^{-1} for 1,4-ADCA, and from 3,667 cm^{-1} to 610 cm^{-1} for 9,10-ADCA (Table 2.1). The quantum yields of 2,6-ADCA and 1,4-ADCA decrease more than an order of magnitude under basic conditions compared to acidic solution, while that of 9,10-ADCA decreases only by about half (Table 2.2).

Table 2.1. Summary of absorption and emission data for the ADCAs

	Solvent	ε^{a}	$\lambda_{\max}^{abs}$ (nm)	$\lambda_{\max}^{em}$ (nm)	Stokes (cm^{-1})	$E_{0,0}$ (eV)
2,6-ADCA	THF	7	409	419	584	3.0
	acidic DMF		409	423	948	3.0
	basic DMF		392	400	510	3.1
1,4-ADCA	THF	7	396	489	4803	2.8
	acidic DMF		390	522	6484	2.8
	basic DMF		396	430	1997	2.9
9,10-ADCA	THF	7	387	451	3667	3.1
	acidic DMF		389	451	3534	3.1
	basic DMF		400	410	610	3.1
Anthracene	THF	7	378	381	208	3.3

[a] ε is the dielectric constant, $\lambda_{\max}^{abs}$ is the lowest energy maximum in the absorbance spectrum, and $\lambda_{\max}^{em}$ is the highest energy maximum in the fluorescence spectrum.

To quantify the degree of protonation in both the ground and excited states as a function of pH, the ground-state acid association constants (*K*) of the ADCAs were determined by absorption spectroscopy (equation S2.1) and p*K* values of 17.6, 17.9 and 19.4, for 2,6-ADCA, 1,4-ADCA and 9,10-ADCA, respectively, were obtained in the ground state. The excited-state acid association constants (p*K**) were then calculated in DMF from the Förster cycle (equation 2.2), and found to be 23.0, 23.2 and 23.8, accordingly. Thus, in neutral solutions, the ADCA derivatives are predominantly protonated in both the ground state and the excited state.

Table 2.2. Summary of the lifetime and quantum yield data for ADCAs

	Solvent	ε^a	τ_f (ns)	τ_0 (ns)	Φ_{fl}	$k_{r,exp}$ ($10^7 s^{-1}$)	$k_{nr,exp}$ ($10^7 s^{-1}$)	$\tau_{0,calc}$ (ns)	$k_{r,calc}$ ($10^7 s^{-1}$)
2,6-ADCA	THF	7	12.1 ± 0.07	22.0 ± 0.08	0.55 ± 0.041	0.045	0.037	--	--
	acidic DMF		15.2 ± 0.2	18.8 ± 0.1	0.81 ± 0.092	0.053	0.013	10.7	0.093
	basic DMF		6.2 ± 0.05	79.5 ± 0.03	0.078 ± 0.019	0.01	0.15	7.6	0.132
1,4-ADCA	THF	7	10.7± 0.1	30.6 ± 0.1	0.35 ± 0.045	0.033	0.061	23.9	0.042
	acidic DMF		12.5 ± 0.1	46.3 ± 0.2	0.27 ± 0.042	0.022	0.058	21.2	0.047
	basic DMF		3.5 ± 0.1	89.8 ± 0.6	0.039 ± 0.021	0.0011	0.27	15.6	0.064
9,10-ADCA	THF	7	8.8 ± 0.3	21.0 ± 0.2	0.42 ± 0.084	0.048	0.066	21.0	0.048
	acidic DMF		8.1 ± 0.7	9.6 ± 0.1	0.84 ± 0.029	0.10	0.020	16.3	0.061
	basic DMF		4.9 ± 1.7	10.4 ± 0.4	0.47 ± 0.035	0.096	0.11	12.6	0.079
Anthracene	THF	7	4.9 ± 0.1	12.3 ± 0.05	0.40 ± 0.010	0.082	0.12	12.6	0.079

[a] ε is the dielectric constant

In addition to solvent polarity and protonation state, geometry can have a significant effect on photophysical properties. DFT and TDDFT calculations were performed to obtain the energies and geometries of the three compounds as a function of the dihedral angles between the carboxylic acid groups and the anthracene ring system (Figure S2.3, Figure S2.4) both in the ground state and in the excited state. The potential energy contours for the 2,6-ADCA isomer in the ground state (Figure 2.2.3) show that the lowest-energy conformation occurs when the carboxylic acids and the anthracene moiety are coplanar. In the excited state, the lowest-energy geometry does not change with respect to the ground state and the molecule remains planar (Figure 2.2.3b). Similar results are obtained for the 1,4-ADCA isomer, where coplanarity of the carboxylic acids and anthracene moieties is observed in both the ground (Figure 2.2.3c) and the first excited state (Figure 2.2.3d). On the other hand, the results for the 9,10-ADCA isomer are strikingly different (Figure 2.2.3e,f). For this isomer, the lowest-energy conformation does not exhibit the carboxylic acids in the same plane as the aromatic rings in either the ground or the first excited state. Full geometry optimizations reveal that the lowest-energy structure for the ground state 9,10-isomer has dihedral angles of 56.6°, and these dihedrals decrease to 27.7° in the first excited state (Figure 2.2.4). Furthermore, the anthracene moiety in the 9-10 isomers seems to undergo a noticeable puckering upon excitation that is completely absent in the other two isomers (Figure 2.2.4).

Close examination of the energy contours in Figure 2.2.3 reveals that, interestingly, there seems to be a lower barrier for carboxyl rotation for 1,4-ADCA than for 2,6-ADCA in the ground state. Indeed, when one of the carboxylic acid groups is coplanar to the anthracene moiety, the barrier for full rotation of the other carboxylic acid group is about 5.5 kcal/mol in 1,4-ADCA, but around 8 kcal/mol in 2,6-ADCA. The most energetically favorable conformations of both 2,6-ADCA and 1,4-ADCA have dihedral angles of $\theta = 0°$ and both have a maximum energy when $\theta = 90°$ (see Figure S2.1 for a definition of the dihedral angles).

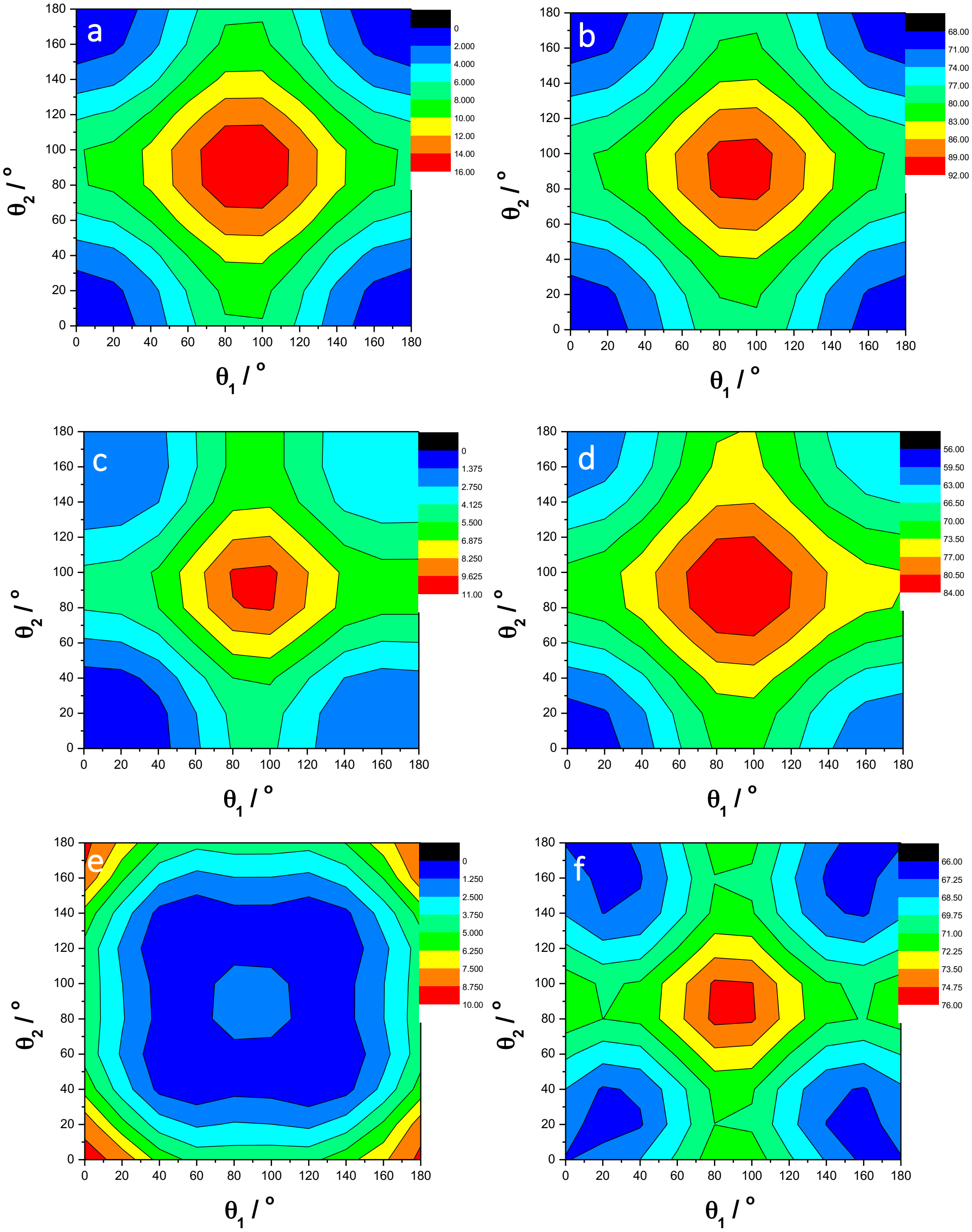

Figure 2.2.3. DFT calculated energies as a function of dihedral angles between –COOH groups and anthracene. Ground state of 2,6-ADCA (a), 1,4-ADCA (c), and 9,10-ADCA (e), and first excited state of 2,6-ADCA (b), 1,4-ADCA (d), and 9,10-ADCA (f). Energy scales for each plot

are shown in kcal/mol relative to the minimum energy of the ground state. (See Figure S2.4 for a definition of the dihedral angles.)

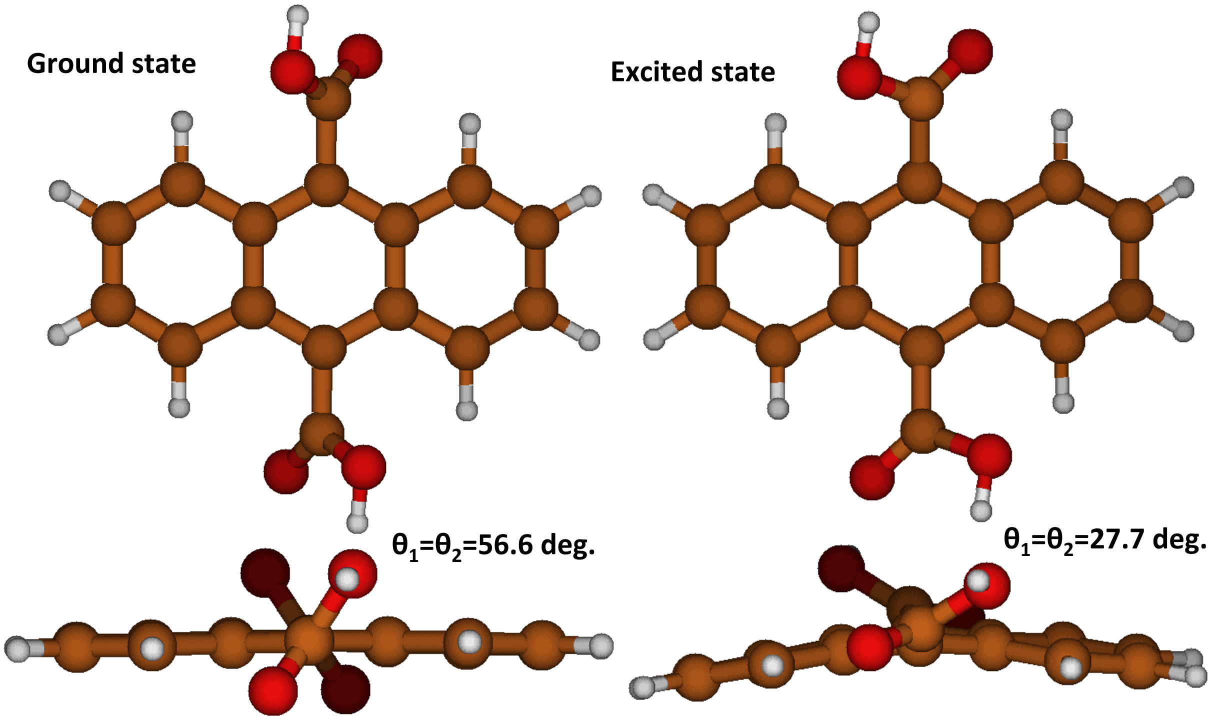

Figure 2.2.4. DFT calculated lowest-energy structures of the 9,10-ADCA molecule in the ground state (left) and the first excited state (right).

2.3. Discussion

As expected, the photophysical characteristics of anthracene are sensitive to the position of the carboxylic acid functionalities on the ring system. Additionally, the protonation state of the acid groups further alters the excited-state properties of each anthracene derivative. The question then becomes, what is the main process that governs the photophysics of each isomer; acid-base equilibrium, solvent, formation of higher order aggregates, or excited-state structural reorganization? Experimentally determined rates of radiative decay can be compared with rates calculated by the Strickler-Berg equation to give insight into the intramolecular and intermolecular interactions that may impact the photophysical properties of the fluorophore. The Strickler-Berg equation (Equation 2.1)[5] extends Einstein's formalism for transition probabilities of atomic absorption and emission to polyatomic molecules. From this equation, the intrinsic lifetime of a molecule, i.e. the radiative lifetime in the absence of intermolecular forces, can be estimated. The Stickler-Berg relation has accurately predicted the lifetimes of a number of molecules; however, it makes a few assumptions that limit its application in certain cases.

$$k_{r,calc} = \frac{1}{\tau_0} = \frac{8\pi\times 2303 c_0 n^2}{N_a} \frac{\int F_v(v_f)dv_f}{\int v_f^3\, F_v(v_f)dv_f} \int \frac{\varepsilon(v_A)dv_A}{v_A}$$

$$= 2.88\times10^{-9} n^2 \frac{\int F_v(v_A)dv_A}{\int v_f^3 F_v(v_f)dv_A} \int \frac{\varepsilon(v_A)dv_A}{v_A} \qquad (2.1)$$

The relationship is based on the Born-Oppenheimer approximation, which assumes that the electronic transition dipole-moment operator does not depend on nuclear coordinates. Furthermore, it assumes that emission occurs only from the lowest-energy excited state. The predictive power of the Strickler-Berg relationship is, therefore, limited by large changes in the nuclear configuration upon generating the excited state, as well as intermolecular interactions between the chromophore and its environment.[34] These latter assumptions are the origin of the discrepancy in this work between the calculated $k_{r,calc}$ obtained from the Strickler-Berg and the experimental $k_{r,exp}$ obtained from the measured fluorescence lifetime and quantum yields of 1,4-ADCA and 9,10-ADCA, while other phenomena are likely responsible for the contradictions for 2,6-ADCA (Table 2.2, Table S2.2).

Neither solvent polarity nor hydrogen bonding character alters the photophysics of 2,6-ADCA. Thus, it is unlikely that intermolecular interactions play a significant role in altering the excited-state properties of the anthracene moiety of this isomer. The absorption spectra of 2,6-ADCA recorded in acidic and neat solvents display distinct vibronic structure, different from that observed in basic solution, which closely resembles the structure of the unsubstituted anthracene molecule. Similar observations have been reported in the absorption spectrum of 2-napthalene carboxylic acid (2-NCA) and 2-anthracenecarboxylic acid (2-ACA).[35] In general, electronic transitions polarized along a given axis are more strongly affected by derivatization of the molecule in the same direction. For example, the dissimilarity of the vibronic bands in the absorption spectrum of 2-ACA compared with anthracene was attributed to stabilization of the $^1A \rightarrow {}^1L_b$ longitudinally polarized low-energy transition. The $^1A \rightarrow {}^1L_b$ transition is weak in unsubstituted anthracene and the corresponding absorption bands are obscured by the more intense $^1A \rightarrow {}^1L_a$ absorption bands. Addition of a second carboxylic acid group, which further extends the length of the molecule, would likely result in greater stabilization of the $^1A \rightarrow {}^1L_b$ transition. Accordingly, the bands assigned to $^1A \rightarrow {}^1L_b$ appear with greater intensity in the absorbance spectrum of 2,6-ADCA. DFT calculations of the lowest energy ground-state configuration of 2,6-ADCA suggest a coplanar arrangement between the carboxylic acids and the anthracene macrocycle (Figure 2.2.3a). This is in agreement with that observed in crystal structures of 2-ACA.[36] The coplanar arrangement allows for resonance interactions between the acid groups and the aromatic ring system to occur. These resonance interactions increase the dipole moment, and thus, the oscillator strength of the $^1A \rightarrow {}^1L_b$ transition, resulting in the appearance of the $^1A \rightarrow {}^1L_b$ bands.[35] The appearance of these strong $^1A \rightarrow {}^1L_b$ transition bands may contribute to the inconsistency between the $k_{r,calc}$ values and the $k_{r,exp}$ values, since the integral of the area under the non-emissive $^1A \rightarrow {}^1L_b$ absorption bands is a component of the Strickler-Berg equation.

The emission spectrum of 2,6-ADCA in neutral and basic solutions is not a mirror image of the absorbance spectrum. Although it displays anthracenic vibronic structure in all solvent conditions, the number of vibronic transitions in the emission is reduced compared to the absorption spectrum. This is not entirely unexpected, as ^1L_a is the only emissive state, and the additional vibronic structure is assumed to be due to absorption into the ^1L_b state.[35] The vibronic structure is indicative of little intermolecular reorganization in the excited state. The slight bathochromic shift in the absorption spectrum relative to anthracene is attributed to inductive effects imposed by the presence of the electron withdrawing functional groups on the polyaromatic ring.

At higher pH values, the carboxylate groups of 2,6-ADCA are less likely to participate in resonance interactions, leading to further decoupling from the aromatic ring system and giving rise to anthracenic vibronic structure in the absorption spectrum.[37] Indeed, the vibronic structure in the absorbance spectrum of deprotonated 2,6-ADCA^{2-} more closely resembles that of anthracene, but is bathochromically shifted ~19 nm relative to anthracene. Thus, the carboxylic acid groups affect the aromatic system through inductive effects but do not participate in resonance interactions when deprotonated.

Contrary to 2,6-ADCA, both the absorption and emission spectra of 1,4-ADCA in neutral solvents lack vibronic structure and are diffuse.[35] Similar observations have been reported for 1-anthracenecarboxylic acid (1-ACA).[35] DFT calculations predict a lowest energy ground state geometry in which the carboxylic acid groups are coplanar with anthracene (Figure 2.2.3c). This conformation increases resonance interactions between the overlapping orbitals of the π-system and carboxyl groups, introducing charge-transfer (CT) character into the $^1A \rightarrow {}^1L_a$ transition (polarized along the short axis) and electron density shifts toward the functionalized ring. The resulting shift of electron density results in loss of vibronic structure in both the absorption and emission spectra. The magnitude of the Stokes shift of 1,4-ADCA increases with the polarity of the solvent, i.e. THF < DMF ≈ DMA. Closer inspection of the spectroscopic data reveals that, as solvent polarity increases, an overall bathochromic shift of ~19 nm is observed in the emission spectrum. Because the carboxyl groups of 1,4-ADCA introduce CT character into the $^1A \rightarrow ^1L_a$ transition, the absorption spectrum is sensitive to solvent interactions with the functional groups. As solvent polarity increases, the excited state is stabilized due to solvent-solute induced dipolar interactions, giving rise to the bathochromic shift observed in the emission spectrum.[35,38] Therefore, solvent relaxation about the weaker excited-state dipole likely contributes to the large Stokes shifts. The coplanar arrangement of the carboxylic acids in the ground state, along with the lack of vibronic structure in the emission spectrum, suggests that the resonance interactions between the carboxylic acids and aromatic ring system in the ground state are conserved in the excited state, which is corroborated by the coplanar lowest-energy structure found in the first excited state (Figure 2.2.3d).

In basic solution, the absorbance spectrum of 1,4-ADCA^{2-} is vibronically structured, while the emission spectrum is still broad and diffuse. Similar observations were reported for 1-ACA^{-}.[35] In both molecules, the deprotonated carboxyl groups do not contribute to resonance forms of the anion in the ground state and consequently, the absorbance spectra are vibronically structured. There are several factors that may contribute to the loss of structure in the emission spectrum. For 1-ACA^{-}, the authors proposed that a shift in electron density upon promotion to the ^1L_a excited state in the direction of the carboxylate group introduces some CT character between the functional group and anthracene moiety, resulting in broadening of the emission spectrum.[35] It is plausible that such phenomena also contribute to the loss of structure observed in the emission spectrum of 1,4-ADCA^{2-}. The Stokes shift of 1,4-ADCA^{2-} (1997 cm^{-1}) is large in comparison with the deprotonated 2,6-ADCA^{2-} (510 cm^{-1}) and 9,10-ADCA^{2-} (610 cm^{-1}). A relatively large change in molecular dipole moment upon excitation would result in such a substantial Stokes shift. Solvent relaxation may also have a significant effect on the fluorescence spectrum. Because the energy of the relaxed excited state is lower than that of the initial Frank-Condon excited state, thermodynamic equilibration with the surrounding solvent would contribute to the loss of structure and bathochromic shift in the emission spectrum of 1,4-ADCA^{2-}. Lastly, it may be possible that the carboxylate groups can easily rotate, which would also give rise to a large Stokes shift (relative to both 2,6-ADCA^{2-} and 9,10-ADCA^{2-}) and broad emission spectrum due to nuclear reorganization. Unfortunately, the excited state geometry of 1,4-ADCA^{2-} could not be predicted computationally, as energy calculations for the deprotonated molecule encountered severe convergence problems.

In neat solvents, the absorption spectrum of 9,10-ADCA displays anthracenic vibronic structure, while the emission spectrum is characterized by a broad, structureless band. Similar observations have been reported for 9-anthracenecarboxylic acid (9-ACA).[41,26,27] The structureless emission of 9-ACA was ascribed to enhanced resonance interactions between the carboxylic acid group and the aromatic moiety, due to rotation of the functional group into the plane of the ring system following excitation.[23]

DFT calculations of the lowest energy configuration ground-state geometry of 9,10-ADCA reveal a dihedral angle of 57° between the carboxylic acid groups and anthracene plane. Comparably, 9-ACA was found to have a dihedral angle of 57° and 88° for the conjugate base, 9-ACA^{-}.[27] This ground-state configuration of 9-ACA is supported by crystallographic data.[42] The non-planar geometry has been attributed to steric interactions between the acid group and the peri-hydrogens on the carbons in the 1 and 8 positions of the anthracene ring.[23] The non-planar orientation prevents resonance interactions between the carboxylate groups and aromatic ring system, and gives rise to anthracene-like vibronic structure in the absorption spectrum. The inductive effects of the electron withdrawing, carboxylic acid groups result in the slight bathochromic shift observed in the absorption spectrum of 9,10-ADCA relative to anthracene. Deprotonation of the carboxylic acids reduces the strength of the inductive effects and consequently, the bathochromic shift in the absorption spectrum of 9,10-ADCA^{2-} is smaller.

TDDFT calculations show that the dihedral angle, θ, decreases to ~28º in the excited state of 9,10-ADCA (Figure 2.2.3f). Interestingly, as the carboxyl groups twist toward a more coplanar orientation, the anthracene ring also puckers. Previously, a θ of ~33º was calculated by TDDFT for 9-ACA in the excited state, but no ring distortion was reported.[27] The distortion of the anthracene plane observed in 9,10-ADCA but not 9-ACA may be due to greater steric strain on the molecule imposed by the additional carboxylic acid. Puckering of the anthracene ring system upon rotation of the carboxyl groups disrupts the transition dipole moment across the short-axis. The large reconfiguration energies associated with this rotation and nuclear reorganization lower the energy of the excited-state, as evidenced by the large Stokes shift observed in the spectra of 9,10-ADCA. The more coplanar orientation allows for overlapping of the p-orbital of the acid group with the π-aromatic system of anthracene, introducing resonance interactions through delocalization of electron density from anthracene into the carboxyl substituents. This significantly perturbs the $^1A \rightarrow {}^1L_a$ transition dipole moment oriented along the short axis of anthracene, giving rise to a broad, structureless emission band. With increased resonance interactions, solvent-solute interactions have a greater contribution to the Stokes shift depending on the rate of rotation of the carboxyl groups relative to the rate of solvent reorganization as intramolecular nuclear reorganization occurs in the excited state. This may be the origin of the large discrepancy in the emission spectrum of 9,10-ADCA in neat DCE compared to that recorded in the other neat solvents (Figure S2.1). The mirror image relationship between the absorption and emission spectra of the fully deprotonated 9,10-ACA^{2-} measured in basic solution indicates that the geometries of the ground and excited states of 9,10-ACA^{2-} are almost identical. Thus, the carboxylate groups remain decoupled from the aromatic system, resulting in vibronically structured emission. This is also supported by DFT/TDDFT calculations, which show little changes between the dihedral angles of 9,10-ADCA^{2-} in the ground (θ = ~50º, Figure S2.4c) and excited (θ = ~60º, Figure S2.4d) states.

2.4. Conclusions

Functionalization of anthracene with carboxylic acid groups results in perturbation of the photophysical properties depending on both the location of the groups and extent of their interaction with the aromatic ring system. In general, functionalization that extends the molecule along the molecular axes containing optical transitions of the same polarization affect the properties of that transition more significantly. For example, derivatization at the 2 and 6 positions extends the molecule along the longitudinal axis and enhances the longitudinally polarized $^1A \rightarrow {}^1L_b$ transition, giving rise to intense $^1A \rightarrow {}^1L_b$ absorption bands. In the 2,6- isomer, electron density remains evenly distributed in the molecule and vibronically structured absorption bands are observed. On the other hand, functionalization at the 1 and 4 positions, which lengthens the molecule along the short axis, gives rise to an uneven distribution of electron density along the polyaromatic ring system and results in broad, diffuse bands in both the absorption and emission spectra. The extent of interaction between the carboxylic acids and the anthracene ring is dictated by how the functional groups are orientated with respect to the anthracene plane. In 1,4-ADCA, the carboxyl groups lie coplanar with the parent anthracene, but in 9,10-ADCA, steric hindrances prevent coplanarity. As a result, there is greater overlap between the p orbitals of the acid groups in the 1 and 4 positions with the π orbitals of anthracene, introducing a greater amount of charge transfer character in 1,4-ADCA compared to 9,10-ADCA. Accordingly, the photophysical properties of 1,4-ADCA are also sensitive to solvent-solute interactions and exhibit a dependence upon solvent polarity. The solvent pH also has a significant influence on the extent to which the functional groups interact with the ring system. In very basic solutions, where the carboxyl groups are completely deprotonated and cannot participate in resonance interactions, vibronically structured bands are observed in the absorbance spectra of all of the ADCA derivatives.

This work provides insight into the structure-property relationship of dicarboxylic anthracene derivatives and their fluorescent properties. An understanding of the effects of substitutions and local environment on the excited-state properties of anthracene can be used to further tune derivatives to obtain desired functionality. Such knowledge will aid in the design of next-generation optoelectronic materials.

2.5. Acknowledgements

This material is based upon work supported by the U.S. Department of Energy, Office of Science, Office of Basic Energy Sciences under Award Number DE-SC0012446. The authors also acknowledge Advanced Research Computing at Virginia Tech for providing computational resources and technical support that have contributed to the results reported within this paper. URL: http://www.arc.vt.edu

2.6. Supplemental Information

2.6.1. Materials

2,6-anthracenedicarboxylic acid (2,6-ADCA), 1,4-anthracenedicarboxylic acid (1,4-ADCA), and 9,10-anthracenedicarboxylic acid (9,10-ADCA) were synthesized following previously reported procedures with minimal modifications and characterized by ^{1}H NMR spectroscopy (-S3).[28,29,30,31,32]

All other chemicals and solvents including anthracene (> 99 %), KOH (85 %), NH_4OH (25-30%), acetic acid (reagent grade > 99%), dimethylformamide (HPLC grade > 99%), dimethylacetamide (spectrophotometric grade > 99%), tetrahydrofuran (ACS grade > 99 %), ethyl acetate (HPLC grade > 99.9%), 1,2-dichloroethane (99.8%), acetone (HPLC grade > 99.5%), and butanone (ACS grade > 99%) were used as received without further purification from Alfa Aesar, Fisher Scientific, or Sigma-Aldrich.

2.6.2. Steady-state absorption spectroscopy

The steady-state absorption spectra of the ADCA derivatives were obtained using an Agilent Technologies 8453 UV-Vis diode array spectrophotometer (1 nm resolution) where the spectra were recorded with samples prepared in a 1 cm quartz cuvette. To determine the extinction coefficients of each compound, three solutions of known concentration were prepared separately, then each was diluted three times. The UV-vis absorbance of each solution was measured and the absorbance at a fixed wavelength was plotted vs. concentration. The extinction coefficient was determined by averaging the slopes of the lines-of-best-fit obtained from each of the three plots.

2.6.3. Steady-state emission spectroscopy and time-resolved emission lifetimes

All samples were prepared at concentrations below 10 μM to reduce aggregation effects. Time-resolved fluorescence lifetimes were obtained via the time-correlated single photon counting technique (TCSPC) with a modified QuantaMaster Model QM-200-4E emission spectrophotometer from Photon Technology, Inc. (PTI) equipped with a 350 nm LED and a Becker & Hickl GmbH PMH-100 PMT detector with time resolution of < 220 ps FWHM.[33] Florescence lifetime decays were deconvoluted from the time-dependent florescence signal and the instrument response function using the fluorescence decay analysis software, DecayFit, available online (Fluortools, www.fluortools.com).

Quantum yields of fluorescence and steady-state emission spectra of the ADCA compounds were measured in ethyl acetate, tetrahydrofuran (THF), 1,2-dichloroethane (1,2-DCE), butanone, acetone, dimethylacetamide (DMA), dimethylformamide (DMF), acidic (acetic acid) DMF and basic (NaOH) DMF. The steady-state emission spectra were obtained using the same QuantaMaster Model QM-200-4E where the sample compartment was replaced with an integrating sphere (PTI). The excitation light source was a 75 W Xe arc lamp (Newport). The detector was a thermoelectrically cooled Hamamatsu 1527 photomultiplier tube (PMT). All measurements were performed in triplicate using three separately prepared solutions of ADCA in each solvent with absorbance values of ~ 0.08-0.09 at the excitation wavelength.

2.6.4. Theoretical calculations

Radiative decay rates were calculated by applying the Strickler-Berg method using the PhotochemCAD 2.1 software. All electronic structure calculations were carried out with the Gaussian 09 suite of programs.[43] The DFT calculations presented in this work were carried out at the B3LYP/6-31G* level. Sample calculations using the M06 density functional, and the larger 6-311G* basis set were used to corroborate key results at the B3LYP/6-31G* level. Ground-state potential-energy contours correspond to relaxed scans in which the relevant dihedral angles between the carboxylic acid groups and the anthracene moiety are allowed to vary at 15° steps while the rest of the coordinates are optimized. Potential-energy contours for the carboxylic acids in the first excited state were obtained using time-dependent B3LYP/6-31G* calculations, directly using the geometries obtained from ground-state dihedral scans.

2.6.5. Determination of acid association constants

Ground-state acid association constants (*K*) of the ADCA derivatives were determined via absorption spectroscopy by monitoring the change in absorption (corrected for dilution) as a function of added acid concentration. Samples of the three acids were prepared in solutions of water with 0, 10 and 30 mol% DMF and were titrated using NaOH and HCl. The absorption value near the isosbestic point at each addition of acid was plotted as a function of acid concentration and the data was fit to Equation 1,

$$A_i = \frac{A_{max}[H^+]^n + A_{min}K}{K + [H^+]^n} \tag{S2.1}$$

where A_i is the absorbance at a given concentration of acetic acid, A_{max} and A_{min} are the absorbance values for the fully protonated and deprotonated species, respectively, *n* is the number of protons associated with a given acid association constant, *K*. A_i values were fit to Equation 1 with *K* as a variable parameter. Fixing *n* to 2 yielded the most reasonable fit of the data. The p*K* values were plotted versus mol% DMF and the p*K* value of each compound in pure DMF was determined by extrapolating to 100 mol% DMF. Excited-state acid association constants (p*K**) were predicted using the Förster cycle, (Equation 2),

$$pK^* - pK = 2.1\times10^{-3}(\overline{v}_{A^-} - \overline{v}_{AH}) \tag{S2.2}$$

$$\overline{v}_{0-0} = \frac{\overline{v}_{max}^{abs} - \overline{v}_{max}^{em}}{2} \tag{S2.3}$$

where $\overline{v}_{A^-}$ and $\overline{v}_{AH}$ correspond to the wavenumber of the 0–0 transitions of A^- and AH, respectively. The wavenumber corresponding to the 0–0 transition was estimated by averaging the wavenumbers at the absorption and emission maxima (Equation 3).[4]

2.6.6. Supplemental Figures and Tables

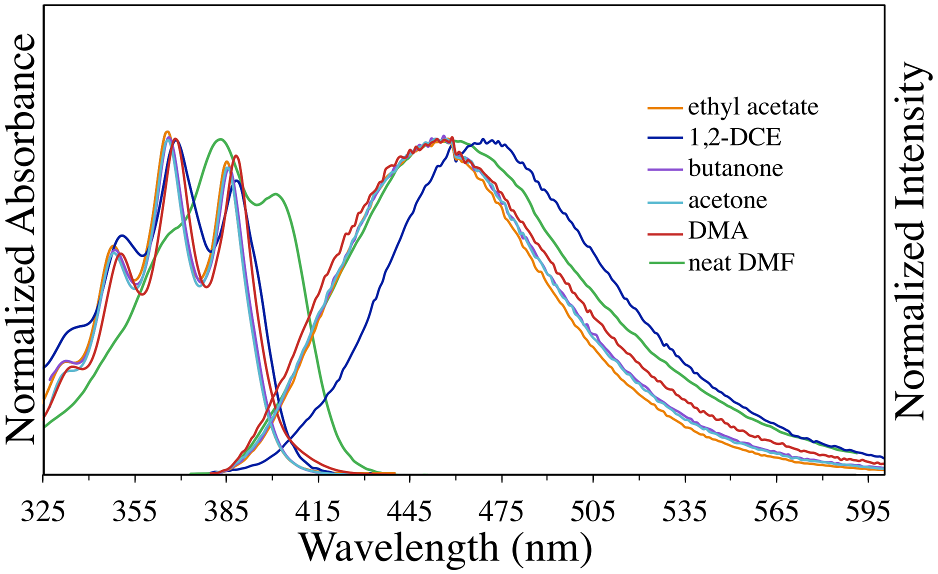

Figure S2.1. Absorption and emission spectra of 9,10-ADCA in ethyl acetate (orange), 1,2-DCE (dark blue), butanone (purple), acetone (light blue), DMA (red) and neat DMF (green).

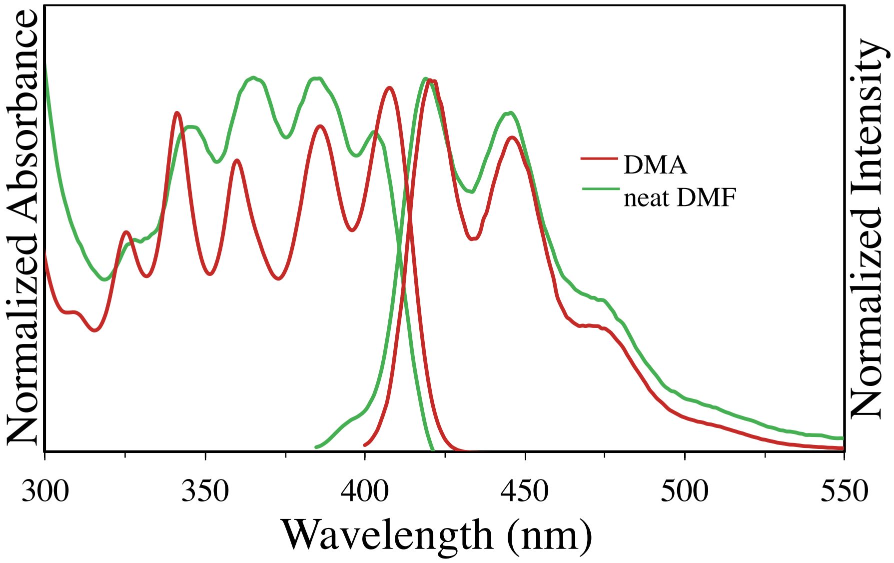

Figure S2.2. Absorption and emission spectra of 2,6-ADCA in neat DMF and DMA

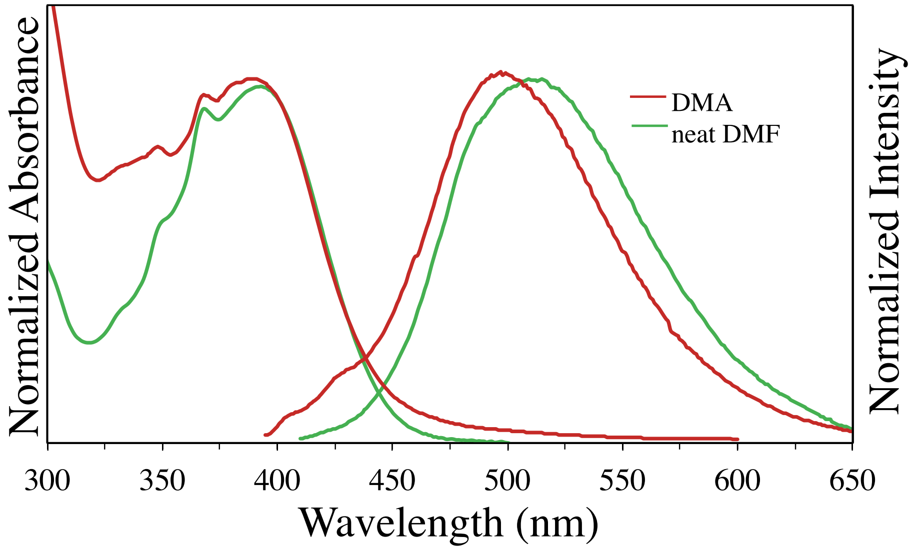

Figure S2.3. Absorption and emission spectra of 1,4-ADCA in neat DMF and DMA

Table S2.1. Absorption and emission yield data of the ADCAs

	Solvent	ε^{α}	$\lambda_{\max}^{abs}$ (nm)	$\lambda_{\max}^{em}$ (nm)	Stokes (cm^{-1})	$E_{0,0}$ (eV)
2,6-ADCA	THF	7	409	419	584	3.0
	DMF	37	403	419	809	3.0
	acidic DMF		409	423	948	3.0
	basic DMF		392	400	510	3.1
1,4-ADCA	THF	7	396	489	4803	2.8
	DMF	37	393	508	5760	2.9
	acidic DMF		390	522	6484	2.8
	basic DMF		396	430	1997	2.9
9,10-ADCA	THF	7	387	451	3667	3.1
	DMF	37	401	454	2911	3.0
	acidic DMF		389	451	3534	3.1
	basic DMF		400	410	610	3.1
Anthracene	THF	7	378	381	208	3.3

Table S2.2. Lifetime and quantum yield data of the ADCAs

	Solvent	ε^{α}	τ_f (ns)	τ_0 (ns)	Φ_{fl}	$k_{r,exp}$ ($10^7 s^{-1}$)	$k_{nr,exp}$ ($10^7 s^{-1}$)	$\tau_{0,calc}$(ns)	$k_{r,calc}$ ($10^7 s^{-1}$)
2,6-ADCA	THF	7	12.1 ± 0.07	22.0 ± 0.08	0.55 ± 0.041	0.045	0.037	--	--
	DMA	38	14.2 ± 0.07	15.3 ± 0.05	0.928 ± 0.045	0.065	0.0054	8.5	0.12
	DMF	37	14.2 ± 0.3	58.9 ± 0.1	0.246 ± 0.028	0.017	0.053	8.3	0.12
	acidic DMF		15.2 ± 0.2	18.8 ± 0.1	0.81 ± 0.092	0.053	0.013	10.7	0.093
	basic DMF		6.2 ± 0.05	79.5 ± 0.03	0.078 ± 0.019	0.01	0.15	7.6	0.132
1,4-ADCA	THF	7	10.7± 0.1	30.6 ± 0.1	0.35 ± 0.045	0.033	0.061	23.9	0.042
	DMA	38	11.5 ± 0.4	29.4 ± 0.1	0.391 ± 0.034	0.034	0.053	18.3	0.055
	DMF	37	9.4 ± 0.3	47.5 ± 1.3	0.198 ± 0.25	0.021	0.085	20.9	0.048
	acidic DMF		12.5 ± 0.1	46.3 ± 0.2	0.27 ± 0.042	0.022	0.058	21.2	0.047
	basic DMF		3.5 ± 0.1	89.8 ± 0.6	0.039 ± 0.021	0.0011	0.27	15.6	0.064
9,10-ADCA	ethyl acetate	6.5	9.1 ± 0.9	47.4 ± 0.3	0.192 ± 0.043	0.021	0.089	12.9	0.078
	THF	7	8.8 ± 0.3	21.0 ± 0.2	0.42 ± 0.084	0.048	0.066	21.0	0.048
	1,2-DCE	10.36	8.4 ± 0.4	32.7 ± 0.1	0.257 ± 0.019	0.31	0.088	--	
	butanone	18.5	9.6 ± 0.2	12.0 ± 0.06	0.802 ± 0.029	0.084	0.020	15.6	0.064
	acetone	21	9.9 ± 0.1	91.7 ± 0.3	0.108 ± 0.035	0.11	0.090	18.9	0.053
	DMA	38	9.7 ± 0.3	29.2 ± 0.09	0.332 ± 0.020	0.34	0.069	13.1	0.076
	DMF	37	6.0 ± 0.2	55.6 ± 0.4	0.108 ± 0.035	0.018	0.15	14.7	0.068
	acidic DMF		8.1 ± 0.7	9.6 ± 0.1	0.84 ± 0.029	0.10	0.020	16.3	0.061
	basic DMF		4.9 ± 1.7	10.4 ± 0.4	0.47 ± 0.035	0.096	0.11	12.6	0.079

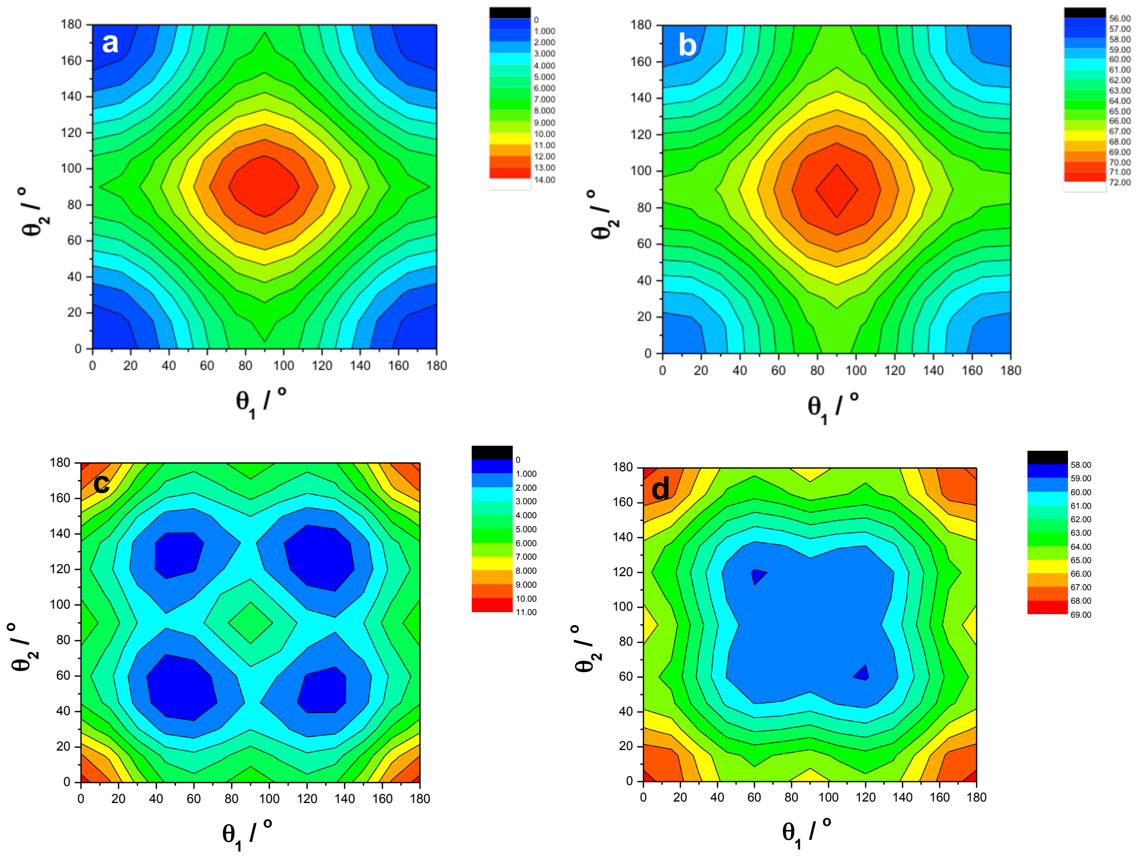

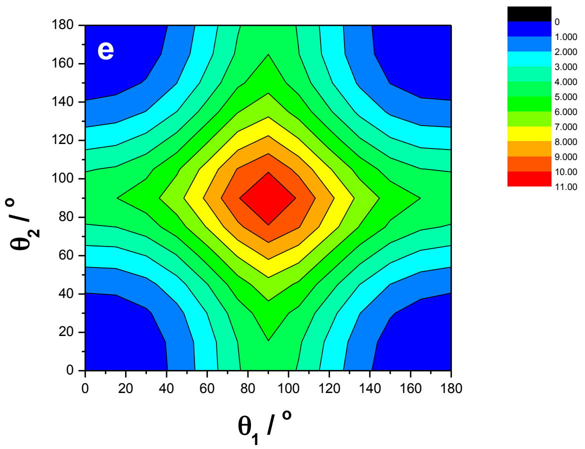

Figure S2.4. DFT calculated energies as a function of dihedral angles between –COOH groups and anthracene. Ground state of 2,6-ADCA^{2-} (a), 9,10-ADCA^{2-} (c) and 1,4-ADCA^{2-} (e) and first excited state of 2,6-ADCA^{2-} (b), and 9,10-ADCA^{2-} (d). Energy scales for each plot are shown in kcal/mol relative to the minimum energy of the ground state. For the 1,4- ADCA^{2-} excited state, calculations did not converge.

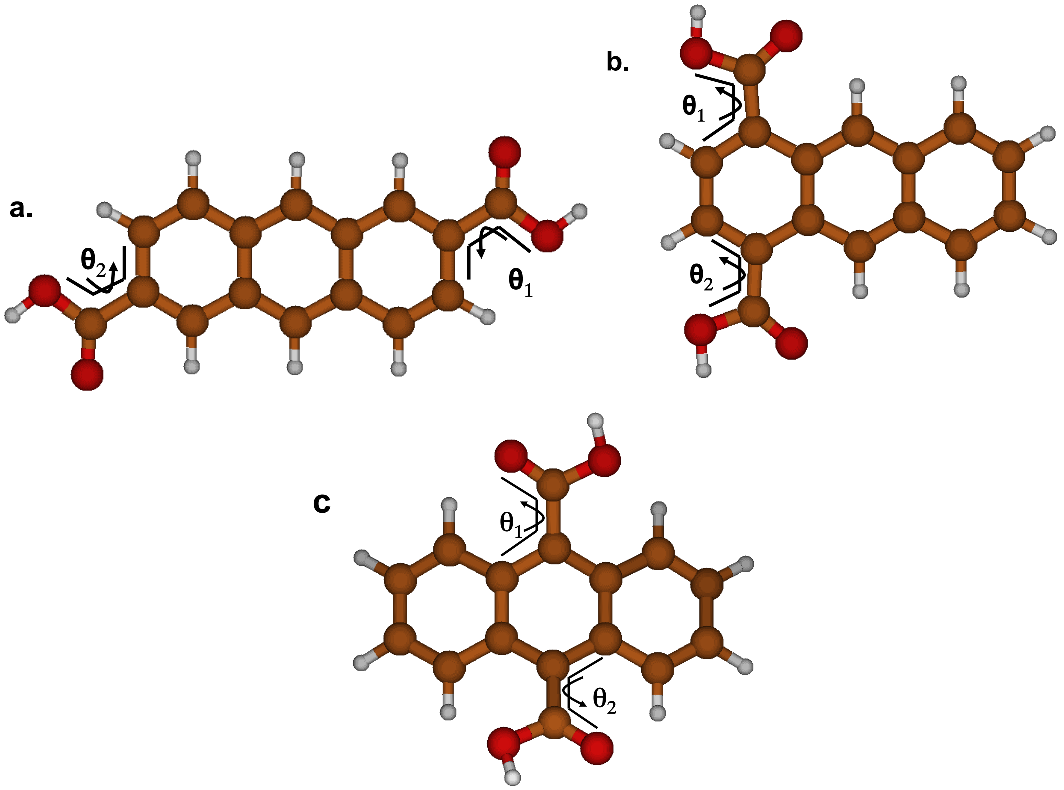

Figure S2.5. Definition of the dihedral angles in Figure 2.2.3 for (a) 2,6-ADCA, (b) 1,4-ADCA, and (c), 9,10-ADCA. Structures in (a) and (b) correspond to the lowest-energy geometries in the ground state. The optimum geometry for 9,10-ADCA is shown in Figure 2.2.4.

2.7. References

1. Zhu, M. Y., C. Blue Fluorescent Emitters: Design Tactics and Applications in Organic Light-Emitting Diodes. *Chem. Soc. Rev.* **2013**, *42*, 4963-4976.
2. Kaur, N. S., M.; Pathakc, D.; Wagner, T; Nunzi, J. M. Organic Materials for Photovoltaic Applications: Review and Mechanism. *Synth. Met.* **2014**, *190*, 20-26.
3. Wakayama, Y. H., R.; Seo, H. S. Recent Progress in Photoactive Field-Effect Transistors. *Sci. Technol. Adv. Mater.* **2014**, *15*, 1019.
4. van de Linde, S. A., S.; Franke, C.; Holm, T.; Klein, T.; Löschberger, A.; Proppert, S.; Wolter, S.; Sauer, M. Investigating Cellular Structures at the Nanoscale with Organic Fluorophores. *Chem. Biol.* **2013**, *20*, 8.
5. Sidman, J. W. Electronic and Vibrational States of Anthracene. *J. Chem. Phys.* **1956**, *25*, 115-121.
6. Shah, B. K. N., D. C.; Shi, J.; Forsythe, E. W.; Morton, D. Photophysical Properties of Anthanthrene-Based Tunable Blue Emitters. *J. Phys. Chem. A.* **2005**, *109*, 7677.
7. Moorthy, J. N.; Venkatakrishnan, P.; Natarajan, P.; Huang, D.-F.; Chow, T. J. De Novo Design for Functional Amorphous Materials: Synthesis and Thermal and Light-Emitting Properties of Twisted Anthracene-Functionalized Bimesitylenes. *J. Am. Chem. Soc.* **2008**, *130*, 17320.
8. Tao, S. X., S.; Zhang, X. Efficient Blue Organic Light-Emitting Devices Based on Novel Anthracene Derivatives with Pronounced Thermal Stability and Excellent Film-Forming Property. *Chem. Phys. Lett.* **2006**, *429*, 622-627.
9. Swager, T. M.; Gil, C. J.; Wrighton, M. S. Fluorescence Studies of Poly(p-phenyleneethynylene)s: The Effect of Anthracene Substitution. The *J. Phys. Chem.* **1995**, *99*, 4886.
10. Platt, J. R. The Box Model and Electron Densities in Conjugated Systems. *J. Chem. Phys.* **1954**, *22*, 4886-4893.
11. Klevens, H. B.; Platt, J. R. Spectral Resemblances of Cata-Condensed Hydrocarbons. *J. Chem. Phys.* **1949**, *17*, 470-483.
12. Platt, J. R. Classification of Spectra of Cata-Condensed Hydrocarbons.. *J. Chem. Phys.* **1949**, *17*, 484-495.
13. Lackowicz, J. R. *Principles of Fluorescence Spectroscopy* 3rd Ed.; Springer Science+Business Media, LLC, 2010; pp 32.
14. Tigoianu, I. R.; Airinei, A.; Dorohoi, D. O. Solvent Influence on the Electronic Fluorescence Spectra of Anthracene. *Rev. Chim. (Bucharest, Rom.)* **2010**, *61*, 491-494.
15. Valeur, B.; Berberan-Santos, M. N. *Molecular Fluorescence: Principles and Applications*; Wiley-VCH, 2012; pp 77.

(16. Berlman, I. B. *Handbook of Fluorescence Spectra of Aromatic Molecules*; 2d ed.; Academic Press: New York, 1971; pp 57-59.

17. Melhuish, W. H. Quantum Efficiencies of Fluorescence of Organic Substances: Effect of Solvent and Concentration of the Fluorescent Solute. *J. Phys. Chem.* **1961**, *65*, 229-235.
18. Ware, W. R.; Baldwin, B. A. Absorption Intensity and Fluorescence Lifetimes of Molecules. *J. Chem. Phys.* **1964**, *40*, 1703.
19. Dawson, W. R.; Windsor, M. W. Fluorescence Yields of Aromatic Compounds. *J. Phys. Chem.* **1968**, *72*, 3251.

20. Lampert, R. A.; Chewter, L. A.; Phillips, D.; O'Connor, D. V.; Roberts, A. J.; Meech, S. R. Standards for Nanosecond Fluorescence Decay Time Measurements. *Anal. Chem.* **1983**, *55*, 68-73.

21. Momiji, I.; Yoza, C.; Matsui, K. Fluorescence Spectra of 9-Anthracenecarboxylic Acid in Heterogeneous Environments. *J. Phys. Chem. B.* **2000**, *104*, 1552-1555.

22. Abdel-Mottaleb, M. S. A.; Galal, H. R.; Dessouky, A. F. M.; El-Naggar, M.; Mekkawi, D.; Ali, S. S.; Attya, G. M. Fluorescence and Photostability Studies of Anthracene-9-carboxylic Acid in Different Media. *Int. J. Photoenergy.* **2000**, *2*, 48-53.

23. Werner, T. C.; Hercules, D. M. Fluorescence of 9-Anthroic Acid and Its Esters. Environmental Effects on Excited-State Behavior. *J. Phys. Chem.* **1969**, *73*, 2005-2011.

24. Suzuki, S.; Fujii, T.; Yoshiike, N.; Komatsu, S.; Iida, T. Absorption and Fluorescence Spectra of Anthracenecarboxylic Acids. I. 9-Anthroic Acid and Formation of Excimer. *Bull. Chem. Soc. Jpn.* **1978**, *51*, 2460-2466.

25. Bazilevskaya, N.; Cherkasov, A. Two Fluorescence Bands of Mesoanthracenecarboxylic Acids and Excimers. *Appl. Spectrosc.* **1965**, *3*, 412-416.

26. Ghoneim, N. Scherrer, D.; Suppan, P. Dual Luminescence, Structure and Eximers of 9-Anthracene Carboxylic Acid. *J. Lumin.* **1993**, *55*, 271-275.

27. Rodriguez-Cordoba, W. N.-M., R.; Navarro, P.; Peon, J. Ultrafast Fluorescence Study of the Effect of Carboxylic and Carboxylate Substituents on the Excited State Properties of Anthracene. *J. Lumin.* **2014**, *145*, 697-707.

28. Cabellero, A. G. C., A. K.; Nalli, S. M. Remote Aromatic Stabilization in Radical Reactions. *Tetrahedron Lett.* **2008**, *49*, 3613-3615.

29. Fontenot, S. A. C., V. M.; Pitt, M. A. W.; Sather, A. C.; Zakharov, L. N.; Berryman, O. B.; Johnson, D. W. Design, Synthesis and Characterization of Self-Assembled As2L3 and Sb2L3 Cyptands. *Dalton Trans.* **2011**, *40*, 12125-12131.

30. Garay, R. O. N., H.; Muellen, K. Synthesis and Characterization of Poly(1,4-anthrylenevinylene). *Macromolecules.* **1994**, *27*, 1922.

31. Jones, N. Dimethyl 9,10-Anthracenedicarboxylate: A Aentrosymmetric Transoid Molecule. **1945**, *67*, 1922-1927.

32. Arient, J. P. *Collect. Czech. Chem. Commun.* Nitration and Oxidation of Anthraquinone Dimethyl Derivatives. **1973**, *39*, 3117.

33. O' Connor, D. V. Phillips, D. *Time–Correlated Single Photon Counting*; Academic Press: London, 1984; pp 36-54.

34. Strickler, S. J.; Berg, R. A. Relationship Between Absorption Intensity and Fluorescence Lifetime of Molecules. *J. Chem Phys.* **1962**, *37*, 814-882.

35. Werner, T. C.; Hercules, D. M. *J. Phys. Chem.* Charge-transfer Effects on the Absorption and Fluorescence Spectra of Anthroic Acids. **1970**, *74*, 1030.

36. Imai, Y.; Murata, K.; Asano, N.; Nakano, Y.; Kawaguchi, K.; Harada, T.; Sato, T.; Fujiki, M.; Kuroda, R.; Matsubara, Y. Selective Formation and Optical Property of a 21-Helical Columnar Fluorophore Composed of Achiral 2-Anthracenecarboxylic Acid and Benzylamine. *Cryst. Growth Des.* **2008**, *8*, 3376-3379.

37. DiCesare, N.; Lakowicz, J. R. Spectral Properties of Fluorophores Combining the Boronic Acid Group with Electron Donor or Withdrawing Groups. Implication in the Development of Fluorescence Probes for Saccharides. *J. Phys. Chem. A.* **2001**, *105*, 6834-6840.

38. Becker, R. S. *Theory and Interpretation of Fluorescence and Phosphorescence*; Wiley Interscience: New York, 1969; pp 175-177.

39. Fitzgerald, L. J.; Gerkin, R. E. Anthracene-1,8-dicarboxylic Acid. *Acta Crystallogr. C.* **1996**, *52*, 1838.
40. Fitzgerald, L. J.; Gerkin, R. E. Anthracene-1-carboxylic Acid. *Acta Crystallogr. C.* **1997**, *53*, 1080.
41. Werner, T. C.; Fisch, R.; Goodman, G. Spectral Studies on Aromatic Esters of 9-Anthroic Acid. *Spectroscopy Lett.* **2006**, *7*, 385.
42. Fitzgerald, L. J.; Gerkin, R. E. Anthracene-9-carboxylic Acid. *Acta Crystallogr. C.* **1997**, 53, 71.
43. Gaussian 09, Revision A.02, Frisch, M. J.; Trucks, G. W.; Schlegel, H. B.; Scuseria, G. E.; Robb, M. A.; Cheeseman, J. R.; Scalmani, G.; Barone, V.; Mennucci, B.; Petersson, G. A.; Nakatsuji, H.; Caricato, M.; Li, X.; Hratchian, H. P.; Izmaylov, A. F.; Bloino, J.; Zheng, G.; Sonnenberg, J. L.; Hada, M.; Ehara, M.; Toyota, K.; Fukuda, R.; Hasegawa, J.; Ishida, M.; Nakajima, T.; Honda, Y.; Kitao, O.; Nakai, H.; Vreven, T.; Montgomery, J. A., Jr.; Peralta, J. E.; Ogliaro, F.; Bearpark, M.; Heyd, J. J.; Brothers, E.; Kudin, K. N.; Staroverov, V. N.; Kobayashi, R.; Normand, J.; Raghavachari, K.; Rendell, A.; Burant, J. C.; Iyengar, S. S.; Tomasi, J.; Cossi, M.; Rega, N.; Millam, J. M.; Klene, M.; Knox, J. E.; Cross, J. B.; Bakken, V.; Adamo, C.; Jaramillo, J.; Gomperts, R.; Stratmann, R. E.; Yazyev, O.; Austin, A. J.; Cammi, R.; Pomelli, C.; Ochterski, J. W.; Martin, R. L.; Morokuma, K.; Zakrzewski, V. G.; Voth, G. A.; Salvador, P.; Dannenberg, J. J.; Dapprich, S.; Daniels, A. D.; Farkas, Ö.; Foresman, J. B.; Ortiz, J. V.; Cioslowski, J.; Fox, D. J. Gaussian, Inc., Wallingford CT, 2009.

3. Photophysical Properties of Zr-based Anthracenic Metal–Organic Frameworks

3.1. Introduction

Metal-organic frameworks (MOFs) are crystalline materials constructed from metal ions or clusters, connected by multidentate organic ligands. In recent years, luminescent MOFs have been investigated for their applications in sensing of small molecule and vapors, light-emitting devices, photocatalysts as well as bioimaging and drug delivery.[1,2] Luminescence in MOFs can arise from lanthanide metal nodes, aromatic organic ligands, metal-to-ligand charge transfer (MLCT) or ligand-to-metal charge transfer (LMCT) interactions or from guest species.[2] MOFs with ligand-based luminescence are advantageous because their optical properties may be fine-tuned by functionalization of the ligand or post synthetic modification.[3] Furthermore, the well-defined crystalline nature of MOFs affords an excellent platform for studying structure-function relationships.[4]

MOFs constructed from luminescent organic ligands often exhibit similar optical properties to that of the free ligand. However, these properties are altered to varying degrees due to coordination to the metal, π–π interactions and/or MLCT or LMCT interactions.[5] A thorough understanding of the excited state properties and how these properties are affected upon incorporation into a MOF is necessary in order to rationally design luminescent MOFs for specific applications. Here in, three anthracene dicarboxylic acid derivatives, 9,10-anthracenedicarboxylic acid (9,10-ADCA), 2,6-anthracenedicarboxylic acid (2,6-ADCA) and 1,4-anthracenedicarboxylic acid (1,4-ADCA) were used to construct the Zr-based MOFs, 9,10-ADC Zr-MOF, 2,6-ADC Zr-MOF and 1,4-ADC Zr-MOF, respectively. Zirconium clusters are known to form highly stable

MOFs due to the strong bonding interactions between Zr^{4+} and the oxygen atoms of the carboxylate linkers.[6,7]

A detailed study of the photophysical properties of these ligands is described in chapter 1 (*vide supra*). Addition of two carboxylic acid groups onto the aromatic ring system distinctively affects the photophysics of the parent anthracene moiety depending on their location and protonation state. Here in, the excited state properties of the three ADC-Zr-MOFs were investigated using stead-state diffuse reflectance and steady-state emission spectroscopies, time-correlated single photon counting (TCSPC) spectroscopy in the solid state and in a solvent suspension and compared to that of the free ligand.

3.2. Results

The 9,10-ADC Zr-MOF was synthesized according to a previously reported procedure modified from UiO-66.[8,9] $ZrCl_4$ (23.3 mg, 0.1 mmol) and 9,10-ADCA (26.6 mg, 0.1 mmol) were added to a 3-dram vial along with DMF (3 mL) and acetic acid (0.6 mL, 120 equivalents). The vial was capped and sealed with Teflon tape and the mixture was ultrasonicated for 15 minutes. The vial was then placed in an oven and heated at 120 ºC for 24 hours. The reaction solution was filtered immediately and a light-yellow powder was collected via vacuum filtration then washed with DMF and ethanol and dried in air.

The 2,6-ADC and 1,4-ADC Zr-MOFs were synthesized using a similar procedure, optimized by changing the concentration of reactants, reaction time, temperature, modulator and amount of modulator used.[10] To prepare the 2,6-ADC Zr-MOF, $ZrCl_4$ (23.3 mg, 0.1 mmol) and 2,6-ADCA (26.6 mg, 0.1 mmol) were added to a 1-dram vial along with DMF (5 mL) and formic acid (60 equivalents). The vial was sealed and the mixture was ultrasonicated for 15 minutes then heated in an oven at 120 ºC for 24 hours. The reaction solution was centrifuged immediately and the solvent was decanted off. The solid was washed with DMF and centrifuged again until the solution was clear. The DMF was decanted off and the solid was dried under vacuum for 3 days. The 1,4-ADC Zr-MOF was prepared by first adding $ZrCl_4$ (23.3 mg, 0.1 mmol), acetic acid (80 equivalents) and DMF (3 mL) in a vial and sonicating for 15 minutes. 1,4-ADCA (26.6 mg, 0.1 mmol) was then added and the solution sonicated again for 15 minutes. The mixture was heated at 100 ºC for 12 hours. The MOFs were obtained by centrifugation, washed with DMF and dried under vacuum.

Figure 3.1.D shows the powder X-ray diffraction (PXRD) patterns of the 9,10-ADC Zr-MOF and the 1,4-ADC Zr-MOF compared to the simulated pattern of UiO-66 obtained from the single-crystal XRD as well as the PXRD pattern of the 2,6-ADC Zr-MOF compared to the simulated pattern of UiO-67. The PXRD patterns were fit to the simulated patterns of UiO-66 and UiO-67 using Le Bail analysis (Figure S3.1, Figure S3.2). As shown in the SEM images (Figure 3.1.A), the 9,10-ADC Zr-MOF forms octahedral crystals of with an average size of ~700 nm. The 2,6-ADC Zr-MOFs also form octahedral crystals ~200 nm in size (Figure 3.1.B). On the other hand, the 1,4-ADC Zr-MOF forms rod-shaped crystals several microns in size (Figure 3.1.C).

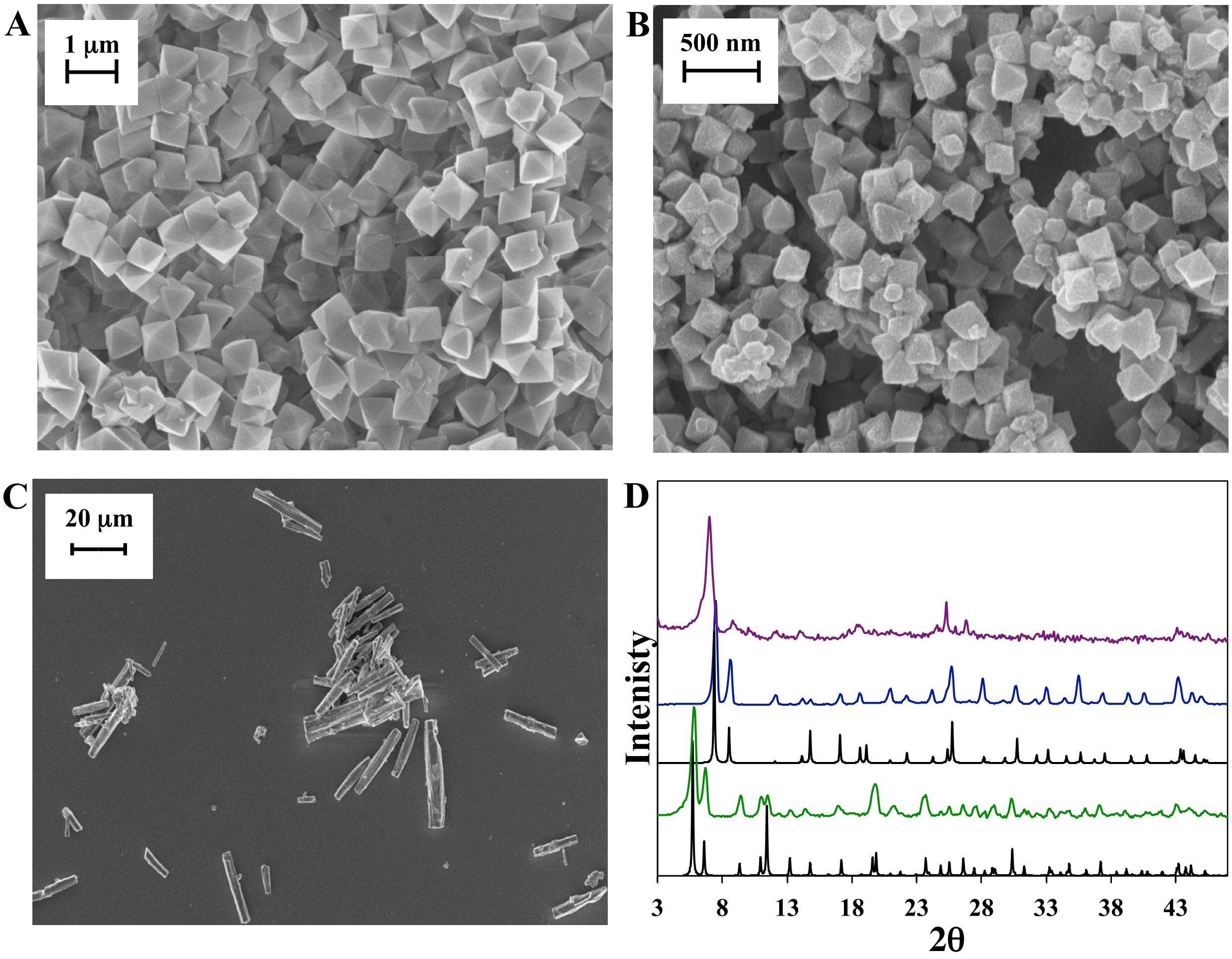

Figure 3.1. SEM images of 9,10-ADCA Zr-MOF (A) 2,6-ADCA Zr-MOF (B) 1,4-ADCA Zr-MOF (C) and PXRD patterns of 1,4-ADCA (purple) 9,10-ADCA (blue) compared to the simulated powder pattern of UiO-66 and 2,6-ADCA (green) compared to the simulated powder pattern of UiO-67.

The absorption and emission spectra of the Zr-MOFs are shown in figure 3.2 along with that of the corresponding protonated (ADCA) and deprotonated (ADC^{2-}) ligands measured in acidic and basic solutions, respectively. Both 9,10-ADCA and 9,10-ADC^{2-} display anthracene-like vibronically structured absorption, while that of 9,10-ADC Zr-MOF is broad and diffuse. The absorption spectrum of the 2,6-ADC Zr-MOF is also significantly broadened compared to that of 2,6-ADCA and 2,6-ADC^{2-}. The bands attributed to the $^1A_1 \rightarrow ^1L_b$ transitions are discernable in the absorption spectrum of the MOF. The 1,4-ADC Zr-MOF displays a diffuse absorption spectrum similar to that of 1,4-ADCA, but is completely unstructured. The absorption spectrum of each of the Zr-MOF is redshifted relative to its free ligand in solution. The absorption spectra of the Zr-MOFs are redshifted 51 nm, 4 nm and 7 nm for 9,10-ADCA, 2,6-ADCA and 1,4-ADCA, respectively, and 41 nm, 21 nm and 27 nm for the deprotonated forms.

The emission spectra of all three Zr-MOFs most closely resemble that of the corresponding protonated linker. The emission spectrum of the 9,10-ADC Zr-MOF is slightly broadened and the emission maximum (λ_{max}) is redshifted by only a few nanometers. The 2,6-ADC Zr-MOF displays vibronically structured emission, analogous to 2,6-ADCA, but is blueshifted by ~ 1 nm. The emission spectrum of the 1,4-ADC Zr-MOF is broad and diffuse, with some slight vibronic features at ~ 405 nm and ~ 425 nm. The λ_{max}, centered at 457 nm, is redshifted 15 nm from that of 1,4-ADCA.

The fluorescence lifetimes of the ADCA Zr-MOFs and ADCA ligands in acidic and basic solution are listed in Table 3.1. The fluorescence decays of the Zr-MOFs were measured in suspensions of the MOF in DMF and were best fit to a biexponential decay function. So far, reasonable, repeatable quantum yield values have not been obtained.

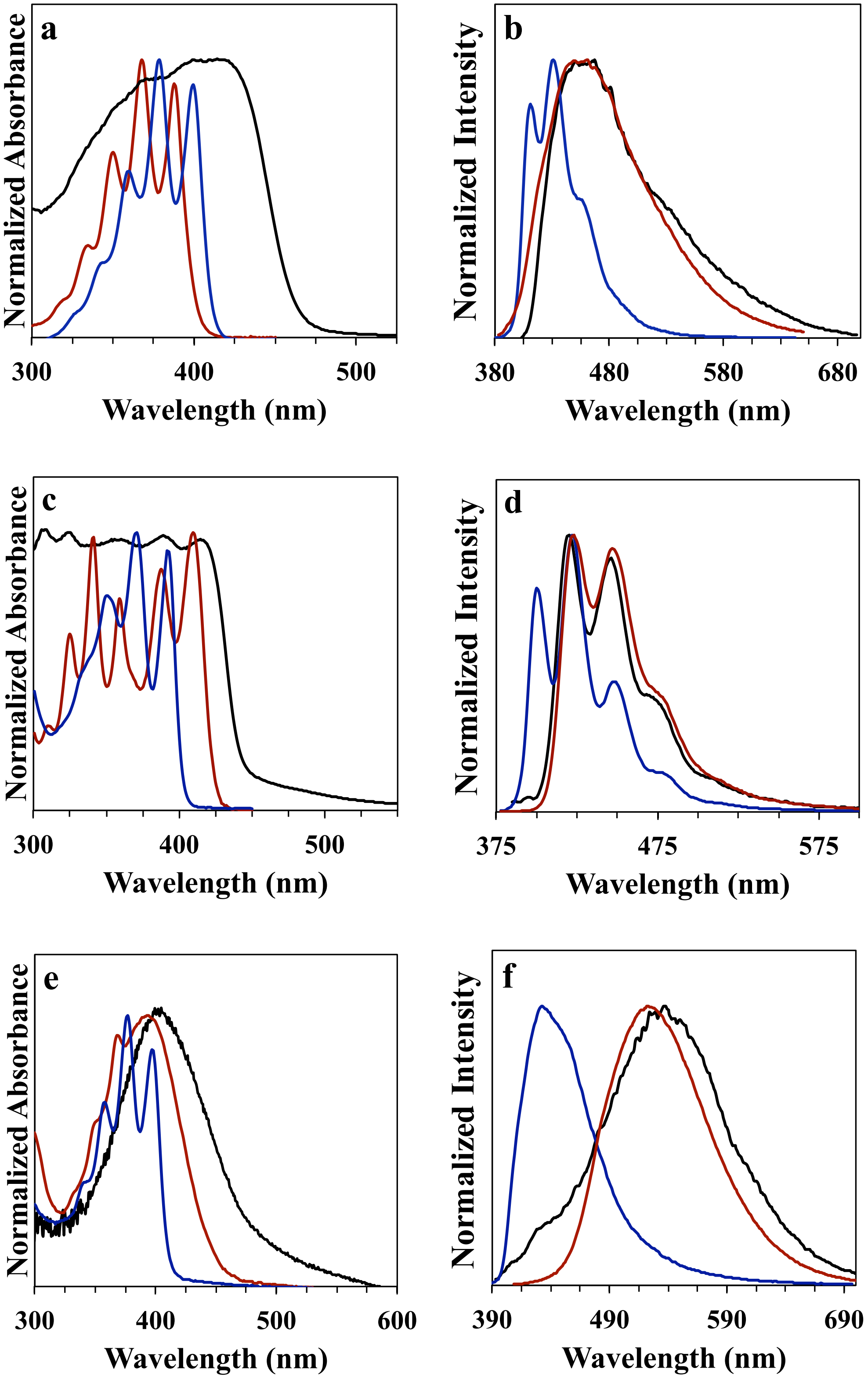

Figure 3.2. Absorption and Emission spectra of 9,10-ADCA (a,b), 2,6-ADCA (c,d) and 1,4-ADCA(e,f) in acidic solution (ADCA, red), basic solution (ADC^{2-}, blue) and in a Zr-MOF (black).

Table 3.1. Absorption and emission data and lifetimes measured for the Zr-MOFs and anthracene-based linkers in solution

	$\lambda_{max,abs}$ (nm)	$\lambda_{max,em}$ (nm)	Stokes (cm^{-1})	$E_{0,0}$ (eV)	τ_1 (ns)	τ_2 (ns)
9,10-ADC Zr-MOF	420	457	1928	2.9	1.1 ± 0.07	6.3 ± 0.06
9,10-ADC^{2-}	379	430	3129	3.1	–	8.1 ± 0.7
9,10-ADCA	369	453	5025	3.1	–	4.9 ± 1.7
2,6-ADC Zr-MOF	393	400	445	3.1	0.2 ± 0.002	14.3 ± 0.2
2,6-ADC^{2-}	410	422	694	3.0	–	15.2 ± 0.2
2,6-ADCA	403	537	6192	2.7	–	6.2 ± 0.05
1,4-ADC Zr-MOF	376	522	7439	2.7	1.7 ± 0.03	8.2 ± 0.09
1,4-ADC^{2-}	420	457	1928	2.9	–	12.5 ± 0.1
1,4-ADCA	379	430	3129	3.1	–	3.5 ± 0.1

3.3. Discussion

The crystal structures of the ADC Zr-MOFs were determined by comparison of the experimental PXRD patterns with the simulated powder patterns of the well-known UiO-66 and UiO-67 frameworks, because MOF crystals large enough for single-crystal X-ray diffraction could not be obtained.[11,12] The PXRD patterns of 9,10-ADC and 1,4-ADC Zr MOFs are compared with that of UiO-66, which is contains 1,4-benzenedicarboxylate (BDC) ligands, since coordination at the 9,10 and 1,4 positions are expected to result in similar spacing between metal nodes. Likewise, the distance between nodes in the 2,6-ADC Zr-MOF would likely be analogous to that of the biphenyl-4,4′-dicarboxylate (BPDC) containing, UiO-67. The peaks observed in the powder patterns of the 9,10-ADC and 2,6-ADC Zr-MOFs match well with the simulated PXRD patterns of UiO-66 and UiO-67, respectively. Le Bail refinements (Figure S3.1, Figure S3.2) of the 9,10-ADC and 2,6-ADC Zr-MOFs are isostructural with the corresponding UiO frameworks and confirmed that no crystalline impurities were present in the sample. Furthermore, the refinements revealed a unit cell lattice size (*a*) of 20.89 Å for the 9,10-ADC Zr MOF and *a* = 26.97 Å for the

2,6-ADC Zr MOF. These values are in good agreement with UiO-66 (a = 20.74 Å) and UiO-67 (a = 26.88 Å).[8,21] Fits of the PXRD pattern obtained for the 1,4-ADC Zr MOF did not converge. However, 2θ of the first peak in the powder pattern of the 1,4-ADC Zr MOF relative to that of 9,10 and 2,6-ADC Zr MOFs, suggests that the unit cell parameter is intermediate the other two MOFs.* The SEM images show that, like UiO-66 and UiO-67, the 9,10 and 2,6-ADC Zr-MOF form octahedral-shaped crystals with high crystallinity. On the other hand, The PXRD pattern obtained for the 1,4-ADC Zr-MOF do not directly correspond to those of UiO-66. Furthermore, the SEM images show that 1,4-ADC Zr-MOFs produced large rod-shaped crystals. This difference could possibly be ascribed to a large degree of defects within the crystal cause by the high steric bulk of the 1,4-ADCA ligand within the UiO-type framework.

To examine the effects on the ground and excited-state properties of the ligands upon coordination into the MOF structure, the photophysics of the Zr-MOFs were compared to that of the protonated (ADCA) and deprotonated (ADC^{2-}) in solution. The redshift and broadening of the emission spectrum of 9,10-ADC and 1,4-ADC Zr-MOFs relative to that of the free ligands is likely caused by interactions with the zirconium ions and/or between anthracene units. Similar broadening and redshift in the emission spectrum of 2,6-naphthalenedicarboxylic acid when incorporated into a Zr-MOFs has previously been reported.[13,14] In one study, DFT calculations revealed that the HOMO/LUMO energy gap of 2,6-naphthalinedicarboxylic acid increases upon coordination to the Zr-oxide nodes and indicated that charge transfer interaction can occur the between the metal ions and aromatic system.[13] Similar interactions between the anthracene-based ligands and Zr-oxide nodes are also likely to occur. Such interactions would result in a broad, redshifted emission spectrum, which is observed for the 9,10-ADC and 1,4-ADC Zr-MOFs.

The substantial degree of broadening and the significant redshift observed in the absorption spectrum may be attributed to intermolecular interactions between the anthracene-based ligands. Such effects are observed in the formation of ground-state anthracene dimers.[15] Additionally, anthracene excimer emission is characterized by a broad emission band in the 400 nm – 700 nm region.[15,16] The magnitude of the effects of π-interactions on the photophysical properties is dependent upon distance between chromophores as well as their orientation. Based on the C–C distance between BDC linkers in UiO-66 of ~ 5.8 Å along with an estimated size of 11.8 Å × 7.8 Å for an anthracene molecule, it is possible for some amount of π-overlap to occur between anthracene moieties of the 9,10-ADC and 1,4-ADC Zr-MOFs.[17,18] Furthermore, the extent of π-overlap should be stronger in the 1,4-ADC Zr-MOF since more of the aromatic anthracene unit is available to interact with neighboring chromophores. Accordingly, a λ_{max} of 457 nm is observed for the 9,10-ADC Zr-MOF and 522 nm for the 1,4-ADC Zr-MOF. It is also likely that a small amount of free ligand may be encapsulated in the pores of the MOF, which would facilitate π-π stacking interactions.

TDDFT calculations of the 9,10-ADCA in the excited-state indicated that the molecule undergoes puckering of the anthracene plane in the excited state due to a decrease in the dihedral angle between the acid groups and the ring system (*vide supra*). The similarity between the emission spectrum of 9,10-ADCA recorded in acidic DMF and in the MOF suggests that the ligand may still undergo such geometry changes within in the MOF.

The 2,6-ADC Zr MOF also displays a broad, redshifted absorption spectrum; however, the emission spectrum appears almost unchanged relative to 2,6-ADCA in solution. The similarity between the vibronic bands in the absorption spectrum of 2,6-ADCA and the 2,6-ADC Zr-MOF indicates that the $^1A_1 \rightarrow {}^1L_b$ transitions polarized along the longitudinal axis are also stabilized in the MOF. In addition, the MOF exhibits emission band with distinct vibronic structure that closely resembles emission of 2,6-ADCA in solution. Therefore, coordination of the 2,6-ADC derivative into the MOF has negligible effects on the $^1A_1 \rightarrow {}^1L_a$ transition, which is responsible for the observed anthracene-based emission (*vide supra*).

The biexponential fluorescence decays measured for all three Zr-MOFs showed a biexponential decay consisting of a longer lifetime component, intermediate of that observed for the corresponding ADCA/ADC^{2-} in solution, as well as a shorter component. There are a few factors that may be responsible for the biexponential decay. First, ground-state interchromophore interactions could result in excimer emission with fluorescence at the same wavelength, resulting in fluorescence from two different species. Alternatively, excited state interaction between chromophore pairs, such as resonance energy transfer, could result in quenched fluorescence from the donor and monomeric emission from the acceptor.[15,19] Because the longest lifetime is very close to that of the free ligand in solution, it is most likely assigned to monomeric emission, as excimer emission generally exceeds that of the monomer. The shorter lifetime is then ascribed to dynamic quenching of ligand-based emission, possibly due to resonance energy transfer from one anthracene unit to another close by.[15,20]

3.4. Conclusions

The photophysics of each of the three anthracene dicarboxylic acids are altered upon coordination to the zirconium-based nodes of the MOFs. Interactions between anthracene units of the linkers further affect their ground and excited-state properties. Moreover, the distances between anthracene units and their orientation within the framework dictate the extent of these intermolecular interactions. In order to better understand chromophores interactions in the MOF, future work will involve obtaining fluorescence quantum yields of the Zr-MOFs as well as transient absorption and emission measurements, unit cell calculations and modifying synthetic parameters in attempt to obtain single-crystals for X-ray diffraction analysis.

3.5. Supplemental Information

3.5.1. Experimental Procedures

3.5.1.1. Materials

2,6-anthracenedicarboxylic acid (2,6-ADCA), 1,4-anthracenedicarboxylic acid (1,4-ADCA), and 9,10-anthracenedicarboxylic acid (9,10-ADCA) were synthesized as described in the previous chapter, and characterized by ^{1}H NMR spectroscopy. All other chemicals and solvents including, $ZrCl_4$, dimethylformamide (HPLC grade > 99%), acetic acid (reagent grade > 99%), and formic acid (reagent grade > 99%) were used as received without further purification from Alfa Aesar, Fisher Scientific, or Sigma-Aldrich.

3.5.2. Powder X-ray diffraction and Scanning electron microscopy

X-ray powder diffraction patterns (PXRD) of MOF powder samples were obtained with a Rigaku Miniflex. SEM images were collected with a Leo/Zeiss 1550 Schottky field emission scanning electron microscope equipped with an in-lens detector.

3.5.3. Steady-state absorption spectroscopy

The steady-state absorption spectra of the ligands were obtained using an Agilent Technologies 8453 UV-Vis diode array spectrophotometer (1 nm resolution) where the spectra were recorded with samples prepared in a 1 cm quartz cuvette. Diffuse reflectance measurements were performed on the same instrument, where the sample compartment was replaced with an integration sphere.

3.5.4. Steady-state emission spectroscopy and time-resolved emission lifetimes

Approximately 3 mg of MOF powder were suspended in 3 mL DMF and the sample was continuously stirred during the emission measurements. All ligand samples were prepared at concentrations below 10 μM to reduce aggregation effects. Time-resolved fluorescence lifetimes were obtained via the time-correlated single photon counting technique (TCSPC) with a modified QuantaMaster Model QM-200-4E emission spectrophotometer from Photon Technology, Inc. (PTI) equipped with a 350 nm LED and a Becker & Hickl GmbH PMH-100 PMT detector with time resolution of < 220 ps FWHM. Florescence lifetime decays were deconvoluted from the time-dependent florescence signal and the instrument response function using the fluorescence decay analysis software, DecayFit, available online (Fluortools, www.fluortools.com).

Quantum yields of fluorescence and steady-state emission spectra of the ADCA compounds were measured in DMF. The steady-state emission spectra were obtained using the same QuantaMaster Model QM-200-4E where the sample compartment was replaced with an integrating sphere (PTI). The excitation light source was a 75 W Xe arc lamp (Newport). The detector was a thermoelectrically cooled Hamamatsu 1527 photomultiplier tube (PMT). All measurements were performed in triplicate using three separately prepared solutions.

To ensure stability of the MOF and the absence of free linker, the solutions were syringe filtered and emission was monitored at the maximum wavelength of emission for each ligand after the emission experiments were completed.

3.5.5. Supplemental Figures

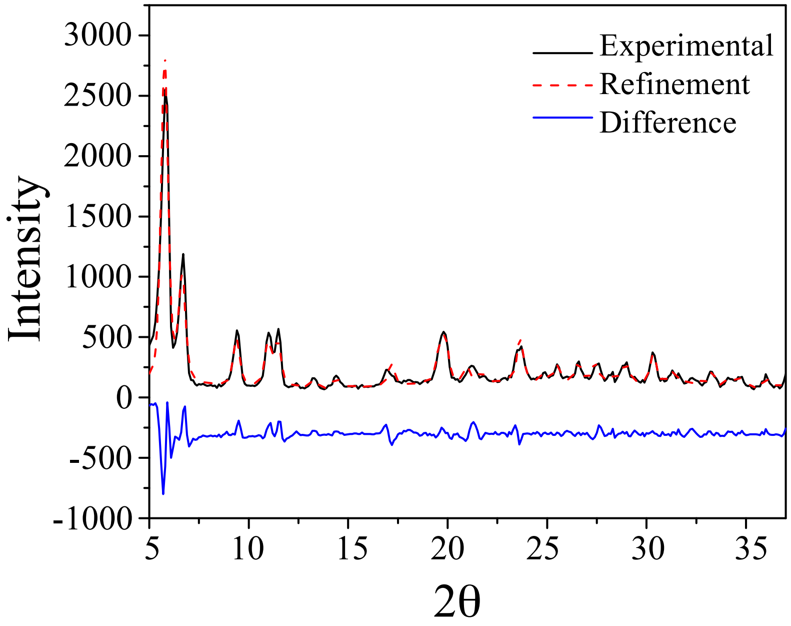

Figure S3.1. Le Bail refinement of the PXRD pattern of the 9,10-ADC Zr-MOF

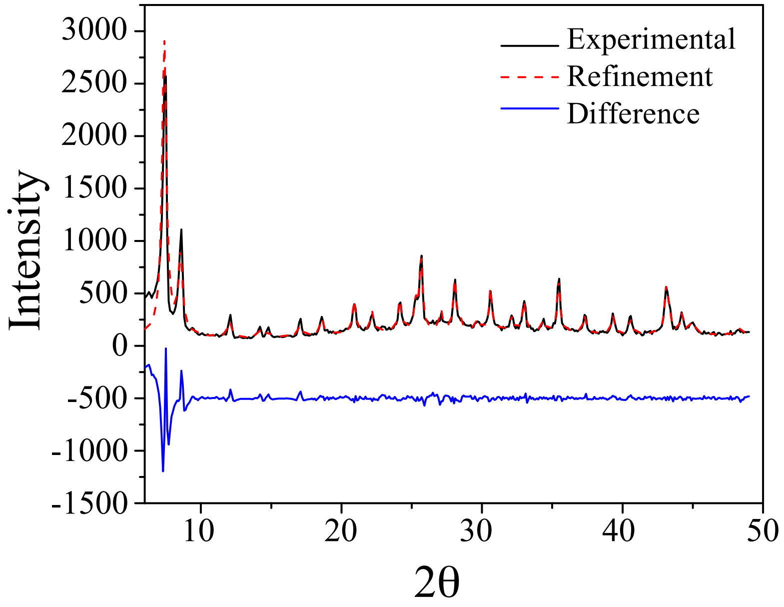

Figure S3.2. Le Bail refinement of the PXRD pattern of the 2,6-ADC Zr-MOF

3.6. References

1. Hu, Z.; Deibert, B. J.; Li, J., Luminescent metal–Organic Frameworks for Chemical Sensing and Explosive Detection. *Chem. Soc. Rev.* **2014,** *43*, 5815–5840.

2. Allendorf, M. D.; Bauer, C. A.; Bhakta, R. K.; Houk, R. J., Luminescent Metal-Organic Frameworks. *Chem Soc Rev* **2009,** *38* (5), 1330-52.

3. Lu, W.; Wei, Z.; Gu, Z. Y.; Liu, T. F.; Park, J.; Park, J.; Tian, J.; Zhang, M.; Zhang, Q.; Gentle, T., 3rd; Bosch, M.; Zhou, H. C., Tuning the Structure and Function of Metal-Organic Frameworks via Linker Design. *Chem Soc Rev* **2014,** *43* (16), 5561-93.

4. Inokuma, Y.; Yoshioka, S.; Ariyoshi, J.; Arai, T.; Hitora, Y.; Takada, K.; Matsunaga, S.; Rissanen, K.; Fujita, M., X-ray Analysis on the Nanogram to Microgram Scale Using Porous Complexes. *Nature* **2013,** *495*, 461-469.

5. Meek, S. T.; Greathouse, J. A.; Allendorf, M. D., Metal-Organic Frameworks: a Rapidly Growing Class of Versatile Nanoporous Materials. *Adv Mater* **2011,** *23* (2), 249-67.

6. Cavka, J. H.; Jakobsen, S.; Olsbye, U.; Guillou, N.; Lamberti, C.; Bordiga, S.; Lillerud, K. P., A New Zirconium Inorganic Building Brick Forming Metal-Organic Frameworks with Exceptional Stability. *J. Am. Chem. Soc.* **2008,** *130* (42), 13850–13851.

7. Bai, Y.; Dou, Y.; Xie, L. H.; Rutledge, W.; Li, J. R.; Zhou, H. C., Zr-Based Metal-Organic Frameworks: Design, Synthesis, Structure, and Applications. *Chem Soc Rev* **2016**.

8. Katz, M. J.; Brown, Z. J.; Colon, Y. J.; Siu, P. W.; Scheidt, K. A.; Snurr, R. Q.; Hupp, J. T.; Farha, O. K., A Facile Synthesis of UiO-66, UiO-67 and Their Derivatives. *Chem Commun (Camb)* **2013,** *49* (82), 9449-51.

9. Pu, S.; Xu, L.; Sun, L.; Du, H., Tuning the Optical Properties of the Zirconium–UiO-66 Metal–Organic Framework for Photocatalytic Degradation of Methyl Orange. *Inorg. Chem. Comm.* **2015,** *52*, 50–52.

10. Schaate, A.; Roy, P.; Godt, A.; Lippke, J.; Waltz, F.; Wiebcke, M.; Behrens, P., Modulated synthesis of Zr-based Metal-Organic Frameworks: From Nano to Single Crystals. *Chemistry* **2011,** *17* (24), 6643-51.

11. Valenzano, L.; Civalleri, B.; Chavan, S.; Bordiga, S.; Nilsen, M. H.; Jakobsen, S.; Lillerud, K. P.; Lamberti, C., Disclosing the Complex Structure of UiO-66 Metal Organic Framework: A Synergic Combination of Experiment and Theory. *Chem Mate.* **2011,** *23* (7), 1700–1718.

12. Chavan, S.; Vitillo, J. G.; Gianolio, D.; Zavorotynska, O.; Civalleri, B.; Jakobsen, S.; Nilsen, M. H.; Valenzano, L.; Lamberti, C.; Lillerud, K. P.; Bordiga, S., H2 Storage in Isostructural UiO-67 and UiO-66 MOFs. *Phys Chem Chem Phys* **2012,** *14* (5), 1614-26.

13. Zhang, W.; Huang, H.; Liu, D.; Yang, Q.; Xiao, Y.; Ma, Q.; Zhong, C., A New Metal–Organic Framework with High Stability Based on Zirconium for Sensing Small Molecules. *Micropor. Mesopor. Mat.* **2013,** *171*, 118–124.

14. Klimov, V. I., Spectral and Dynamical Properties of Multiexcitons in Semiconductor Nanocrystals. *Annu Rev Phys Chem* **2007,** *58*, 635-73.

15. Melo, J. S. S.; Costa, T.; Castroa, C. S.; Macanita, A. L., Photochemistry. In *Photophysics of Fluorescently Labeled Pligomers and Polymers* [Online] 2013.

16. Valeur, B.; Berberan-Santos, M. N., *Molecular Fluorescence: Principles and Applications*. Wiley-VCH: 2012.

17. Hong, D. H.; Suh, M. P., Enhancing CO2 Separation Ability of a Metal-Organic Framework by Post-Synthetic Ligand Exchange with Flexible Aliphatic Carboxylates. *Chemistry* **2014,** *20* (2), 426-34.

18. Jas, G. S.; Wang, Y.; Pauls, S. W.; Johnson, C. K.; Kuczera, K., Influence of Temperature and Viscosity on Anthracene Rotational Diffusion in Organic Solvents: Molecular Dynamics Simulations and Fluorescence Anisotropy Study. *J. Chem. Phys.* **1997,** *107* (21), 8800–8812.

19. Tohnai, N., Luminescence Modulation of Organic Crystals by a Supramolecular Approach. In *Advances in Organic Crystal Chemistry: Comprehensive Reviews 2015*, Tamura, R.; Miyata, M., Eds. Springer Japan: Tokyo, 2015; pp 569-586.

20. Hinoue, T.; Shigenoi, Y.; Sugino, M.; Mizobe, Y.; Hisaki, I.; Miyata, M.; Tohnai, N., Regulation of pi-Stacked Anthracene Arrangement for Fluorescence Modulation of Organic Solid from Monomer to Excited Oligomer Emission. *Chemistry* **2012,** *18* (15), 4634-43.

21. Qingyuan, Y.; Vincent, G.; Florence, R.; Andrew, D. W.; Philip, L. L.; Chongli, Z.; Thomas, D.; Christian, S.; Guillaume, M., CH4 Storage and CO2 Capture in Highly Porous Zirconium Oxide Based Metal–Organic Frameworks. *Chem. Commun* **2012**, *48*, 9831–983.